

A macro-modelling continuum approach with embedded discontinuities for the assessment of masonry arch bridges under earthquake loading

B. Pantò^{a,b,*}, S. Grosman^a, L. Macorini^a, B.A. Izzuddin^a

^a Department of Civil and Environmental Engineering, Imperial College London, South Kensington Campus, London SW7 2AZ, UK

^b Department of Engineering, Durham University, Durham, UK

ARTICLE INFO

Keywords:

Seismic analyses
Environmental actions
Earthquake engineering
Finite element method
Mesoscale models
Macroscale finite element models
Nonlinear dynamic analyses
Historical bridges

ABSTRACT

The paper presents a novel effective macro-modelling approach for masonry arches and bridges under cyclic loading, including dynamic actions induced by earthquakes. It utilises an anisotropic material model with embedded discontinuities to represent masonry nonlinearities. Realistic numerical simulations of masonry arch bridges under static and dynamic loading require accurate models representing the anisotropic nature of masonry and material nonlinearity due to opening and closure of tensile cracks and shear sliding along mortar joints. The proposed 3D modelling approach allows for masonry bond via simple calibration, and enables the representation of tensile cracking, crushing and shear damage in the brickwork. A two-scale representation is adopted, where 3D continuum elements at the structural scale are linked to embedded nonlinear interfaces representing the *meso*-structure of the material. The potential and accuracy of the proposed approach are shown in numerical examples and comparisons against physical experiments on masonry arches and bridges under cyclic static and dynamic loading.

1. Introduction

Masonry arch bridges are old structures which still play a crucial role within modern railway and roadway networks. The vast majority of existing masonry bridges were built more than one hundred years ago mostly following empirical rules [1], and in many cases they date back to the medieval or Roman times representing important architectural heritage assets for numerous countries worldwide. Since their construction, they have been subjected to environmental actions causing progressive material degradation eventually leading to a reduction of the structural performance [2,3].

In general, masonry bridges show a very complex 3D response under traffic and extreme loading. It is governed by material nonlinearity in masonry, which in turn depends upon the properties of units and mortar joints and the bond pattern, and by the interaction among the different bridge components including arch, backfill, spandrel walls and piers in the case of multi-span bridges. Under dynamic loads, such as those induced by earthquakes, the response is determined also by mechanical degradation with reduction of strength and stiffness of masonry due to opening and closure of tensile cracks and shear sliding along the mortar joints, by energy dissipation associated with the hysteretic behaviour of

the backfill, and by the free-field conditions at the bridge boundaries.

Despite an increasing attention from the scientific community towards the behaviour of masonry arch bridges over the past three decades, many aspects concerning the cyclic and dynamic response of these complex structural systems are yet to be fully explored. Thus far, most of the research has been devoted to studying masonry bridges under static forces representing gravity and traffic loading. Laboratory tests were performed to investigate the load capacity of arch bridges [4] evaluating the influence of backfill [5–8], spandrel and wing walls [9], and degradation phenomena associated with masonry bond, such as ring separation in multi-ring arches [10–12]. On the other hand, very limited experimental studies focused on the response of masonry arches and vaults under horizontal cyclic loading [13] and dynamic actions [14], while the dynamic behaviour of masonry arch bridges under earthquake loading has yet to be investigated in physical tests.

On the numerical modelling front, masonry bridges are usually assessed employing 2D models based upon limit analysis concepts [15–17], the finite element method [18,19] or discrete element approaches [20,21]. 2D descriptions generally entail a limited computational cost so they are suitable for practical assessment also of large bridges, but they cannot represent transverse behaviour induced by eccentric or lateral loading and the 3D interaction between the different

* Corresponding author at: Department of Engineering, Durham University, Durham, DH1 3LE, UK.

E-mail address: bartolomeo.panto@durham.ac.uk (B. Pantò).

<https://doi.org/10.1016/j.engstruct.2022.114722>

Received 17 December 2021; Received in revised form 18 June 2022; Accepted 22 July 2022

Available online 20 August 2022

0141-0296/© 2022 The Authors. Published by Elsevier Ltd. This is an open access article under the CC BY license (<http://creativecommons.org/licenses/by/4.0/>).

Notation	
<i>Latin upper case letters</i>	
C	Internal kinematics compatibility matrix
D	Damage matrix
D_n	Damage index in the normal direction
D_t	Damage index in the shear direction
E_b	Young's modulus of bricks
E_m	Young's modulus of mortar
E_n	Homogenised normal modulus
E_t	Homogenised shear modulus
F_s	Yield surface in shear
F_t	Yield surface in tensile
F_c	Yield surface in compression
G_s	Shear fracture energy
G_t	Tensile fracture energy
G_c	Compression fracture energy
K	Macroscopic tangent stiffness matrix
\mathbf{K}_{int}	Tangent stiffness matrix at the local level
E	Tangent stiffness matrix of a single Internal Layer
\mathbf{E}_0	Elastic stiffness matrix of a single Internal Layer
<i>Latin lower case letters</i>	
b, h	Dimensions of the bricks
h_z	Height of the bricks
h_m	Average thickness of bed and head joints
h_{mz}	Thickness of circumferential joints
c	Cohesion
\mathbf{d}	Internal Layer strain vector
\mathbf{d}_p	Internal Layer plastic strain vector
\mathbf{d}_{int}	Strain vector at the local level
g_s	Shear plastic potential
f_t	Tensile strength
f_c	Compression strength
h_{bw}	Bandwidth length
k_n	Normal stiffness of the mesoscale interfaces
k_t	Shear stiffness of the mesoscale interfaces
q	Hardening parameter of the damage-plasticity constitutive model
\mathbf{s}	Internal Layer stress vector
\mathbf{s}_{int}	Stress vector at the local level
$\tilde{\mathbf{s}}$	Internal Layer effective stress vector
<i>Greek upper case letters</i>	
Γ_k	Internal layer (IL) normal to the local k direction ($k = x, y, z$)
<i>Greek lower case letters</i>	
$\boldsymbol{\varepsilon}$	Macroscopic strain vector
$\boldsymbol{\sigma}$	Macroscopic stress vector
$\boldsymbol{\varepsilon}_p$	Macroscopic plastic strain vector
α_{hk}	Parameter linking the macroscopic shear strains to the shear strains of the internal layers ($hk = xy, xz, yz$)
ν_b	Poisson's coefficient of bricks
ν_m	Poisson's coefficient of mortar
ϕ	Friction coefficient
ϕ_g	Dilatancy coefficient
μ	Model parameter of the damage-plasticity constitutive model governing the closure of the tensile cracks

bridge components. To overcome these limitations, 3D modelling strategies with different levels of detail and accuracy have been developed [22–29], where the behaviour under earthquake loading has been studied mainly using FE continuum approaches with macroscale material descriptions for masonry [24,30,31]. In these models, masonry is simulated by an equivalent homogeneous material and isotropic smeared-crack nonlinear constitutive laws, assuming plastic yield domains defined in terms of principal stresses, such as the total strain rotating crack model (TSRCM) implemented in DIANA FEA [32]. This model describes the tensile and compressive behaviour of the material employing a uniaxial stress–strain relationship and assuming that the crack directions rotate with the principal strain axes. Homogeneous finite element approaches have the advantage of requiring a limited computational effort, as the mesh size is independent from the actual masonry bond and the dimensions of the units. However, such macroscale material models bring important limitations, as they do not consider the anisotropy nature of brick/block masonry and do not allow for realistic damage accumulation under cyclic loading. Moreover, studies conducted on masonry buildings [33], and masonry bridges [34] showed that macroscale isotropic models require complex calibration procedures to simulate the realistic brick/block-masonry response under monotonic or cyclic loading conditions. In this regard, advanced 3D homogeneous techniques have been proposed to describe the nonlinear response of masonry walls and curved masonry elements including skew arches allowing for the actual bond [35]. As an alternative to continuous homogenised FEM approaches, *meso*-macro models [36] with advanced two-step homogenisation techniques [37,38], or discrete approaches [27,39,40] have been employed to assess curved structures and masonry arch bridges.

This paper investigates the cyclic and dynamic behaviour of masonry arches by employing a novel continuum macro-modelling strategy, which has been recently developed and employed to simulate the in-

plane and out-of-plane response of masonry walls [41], and here it is applied for the first time to investigate masonry arches and bridges. The results of the numerical study have been used (i) to assess the accuracy of the proposed macro-modelling strategy via comparisons against experimental and detailed mesoscale masonry models and (ii) to investigate the dynamic behaviour of masonry bridges and the complex interaction between masonry and backfill components under cyclic loading conditions.

The proposed continuum model allows for masonry anisotropy by means of discrete embedded interfaces describing the response at the local level, while a continuum Cauchy representation is adopted at the macroscale. A simple but robust multi-scale approach is adopted to transfer information from the macroscale to the local level and *vice versa*. This modelling strategy enables a practical model calibration through the direct use of mesoscale mechanical parameters, and it achieved a drastic reduction of the computational burden when applied to large structures, especially in comparison with detailed mesoscale approaches [25,26]. The ability of the proposed continuum macroscale description to predict the cyclic and dynamic response of masonry arches and bridges is evaluated considering 2D and 3D arch specimens, also interacting with backfill, and assuming as reference solutions the results from detailed mesoscale simulations. Parametric analyses are also performed to identify the most critical material parameters governing the hysteretic behaviour of the analysed systems.

2. Macromodel with embedded discontinuities

The proposed macro-modelling strategy is based on a two-scale description of the masonry material. At the macro level, the masonry is simulated as an equivalent homogenised continuum material, discretised by means of a standard mesh of solid finite elements, while, at the local level, the *meso*-structure of the material is described by means of a

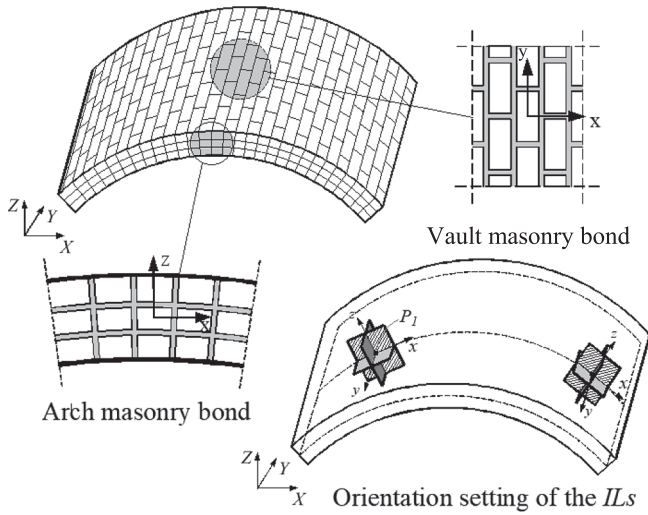


Fig. 1. Orientation of the local layers according to the vault and arch masonry bond.

uniform distribution of discontinuities, hereinafter referred to as *internal layers (ILs)*. The ILs represent embedded interfaces, which allow spreading the plastic flow and damage (in real structures mostly concentrated at the mortar joints) uniformly into the material volume. As a result, at each Gauss integration point of an element domain, three ILs are considered ($\Gamma_x, \Gamma_y, \Gamma_z$), whose normal directions are along the main local material directions (x, y, z in Fig. 1) corresponding to the orientations of the mortar joints within the brick/blockwork. The orientation of the ILs, with reference to a multi-ring barrel vault, is schematically depicted in Fig. 1. More specifically, the local z axis corresponds to the direction of the circumferential mortar joints connecting adjacent rings, while the x and y axes are set along the bed and head joints of the masonry vault. This allows the macro-model to effectively simulate the 3D anisotropic nature of the material, also in presence of double-curvature or irregular geometries such as skew arch textures [39].

According to the proposed modeling strategy, a Cauchy continuum strain field in the local reference system, $\boldsymbol{\varepsilon} = [\varepsilon_x \ \varepsilon_y \ \varepsilon_z \ \gamma_{xy} \ \gamma_{xz} \ \gamma_{yz}]^T$, describes the deformations at the macro level. The macroscopic strains are transferred to the mesoscale level at each Gauss point of the domain (P in Fig. 2) and used to compute the deformations of the internal layers $\mathbf{d}_k = [d_k \ d_{kh} \ d_{kh}]^T$ ($k = x, y, z; h = x, y, z$ with $h \neq k$) composed of one normal component (d_k) and two shear components (d_{kh}) on the plane with normal k .

The dual local stresses of the ILs $\mathbf{s}_k = [s_k \ s_{kh} \ s_{kh}]^T$ are linked to the local strains by the incremental relationship $\delta \mathbf{s}_k = \mathbf{D}_k \delta \mathbf{d}_k$, where \mathbf{D}_k is the tangent stiffness matrix associated with the plane Γ_k . The complete sets of local strains and stresses are ordered in the 9-components vectors \mathbf{d}_{int} and \mathbf{s}_{int} :

$$\mathbf{d}_{int} = [d_x \ d_y \ d_z \ d_{xy} \ d_{xz} \ d_{yz} \ d_{yx} \ d_{zx} \ d_{zy}]^T \quad (1)$$

$$\mathbf{s}_{int} = [s_x \ s_y \ s_z \ s_{xy} \ s_{xz} \ s_{yz} \ s_{yx} \ s_{zx} \ s_{zy}]^T \quad (2)$$

Simple kinematic compatibility relationships are utilised to link the local strains (\mathbf{d}_{int}) to the macroscopic strains ($\boldsymbol{\varepsilon}$), as expressed by:

$$\delta \mathbf{d}_{int} = \begin{bmatrix} 1 \\ 1 \\ 1 \\ \alpha_{xy} & 1 - \alpha_{xy} \\ \alpha_{xz} & 1 - \alpha_{xz} \\ \alpha_{yz} & 1 - \alpha_{yz} \end{bmatrix} \delta \boldsymbol{\varepsilon} \quad (3)$$

By imposing the Cauchy equilibrium conditions, namely the internal rotational equilibrium between the corresponding shear stress

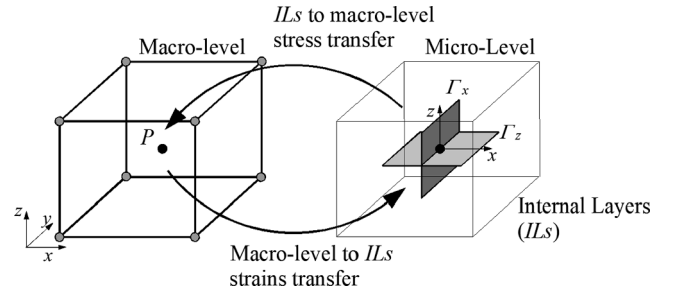


Fig. 2. Schematic representation of the double-scale description adopted in the macro-model.

components ($\tau_{kh} = \tau_{hk}$), it is possible to evaluate the parameters α_{xy} , α_{xz} and α_{yz} corresponding to the increment of macroscopic strains ($\delta \boldsymbol{\varepsilon}$), and thus the relation linking the increment of the internal strains to the increment of the macroscopic strains [41]:

$$\delta \mathbf{d}_{int} = \begin{bmatrix} \mathbf{I}_{3 \times 3} & \mathbf{0}_{3 \times 3} \\ -\mathbf{A}^{-1} \mathbf{B} \\ [\mathbf{0}_{3 \times 3} & \mathbf{I}_{3 \times 3}] + \mathbf{A}^{-1} \mathbf{B} \end{bmatrix} \bullet \delta \boldsymbol{\varepsilon} = \mathbf{C} (\mathbf{D}_x, \mathbf{D}_y, \mathbf{D}_z) \bullet \delta \boldsymbol{\varepsilon} \quad (4)$$

where:

$$\mathbf{A} = \begin{bmatrix} S_{x,22} + S_{y,22} & S_{x,23} & -S_{y,23} \\ S_{x,32} & S_{x,33} + S_{z,22} & S_{z,23} \\ -S_{y,32} & S_{z,32} & S_{y,33} + S_{z,33} \end{bmatrix} \quad (5)$$

$$\mathbf{B} = \begin{bmatrix} S_{x,21} & -S_{y,21} & 0 & -S_{y,22} & 0 & 0 \\ S_{x,31} & 0 & -S_{z,21} & 0 & -S_{z,22} & -S_{z,23} \\ 0 & S_{y,31} & -S_{z,31} & S_{y,32} & -S_{z,32} & -S_{z,33} \end{bmatrix} \quad (6)$$

As can be observed from Eq. (4), the kinematics compatibility matrix (\mathbf{C}), linking the macroscopic and local strains, depends on the tangent stiffness matrix of the ILs. As a result, the procedure is iterative. In the numerical application, a full Newton-Raphson scheme is adopted until the internal equilibrium is reached [41]. At each iteration, Eq. (4) is used to perform the elastic prediction phase, while the plastic correction is carried out by integrating independently the constitutive laws of the three ILs and evaluating the residual unbalance vector for the next iteration. From the compatibility relation in Eq. (4), the macroscopic stress $\boldsymbol{\sigma} = [\sigma_x \ \sigma_y \ \sigma_z \ \tau_{xy} \ \tau_{xz} \ \tau_{yz}]^T$ can be written as reported in Eq. (7a). Alternatively, when Cauchy equilibrium condition are satisfied, the macroscopic stress can be obtained directly by Eq. (2), leading to Eq. (7b).

$$\boldsymbol{\sigma} = \mathbf{C}^T \bullet \mathbf{s}_{int} \quad (7a)$$

$$\boldsymbol{\sigma} = [\mathbf{I}_{6 \times 6} \ \mathbf{0}_{6 \times 3}] \bullet \mathbf{s}_{int} \quad (7b)$$

When local convergence is reached, the local macroscopic tangent stiffness matrix (\mathbf{K}), which is required for determining the increment of nodal displacement within the FE solution procedure, is evaluated by imposing the virtual work principle resulting in:

$$\mathbf{K} = \mathbf{C}^T \bullet \mathbf{K}_{int} \bullet \mathbf{C} + \partial \mathbf{C}^T / \partial \boldsymbol{\varepsilon} \bullet \mathbf{s}_{int} \quad (8a)$$

where \mathbf{K}_{int} is the local tangent stiffness matrix containing the tangent stiffness matrices of the three internal layers. Given that \mathbf{s}_{int} satisfies the Cauchy equilibrium condition and considering Eqs. (7), it follows $\mathbf{C}^T = [\mathbf{I}_{6 \times 6} \ \mathbf{0}_{6 \times 3}]$. Therefore, the variation in the second term in Eq. (7) is zero, and the tangent stiffness matrix can be written as:

$$\mathbf{K} = \mathbf{C}^T \bullet \mathbf{K}_{int} \bullet \mathbf{C} \quad (8b)$$

3. Macromodel calibration

In this work, the damage-plasticity material model developed by Minga et al. [42] is adopted to describe the mechanical behaviour of the ILs. This underlying constitutive model considers three strain-stress components: $\mathbf{s} = [\sigma \ \tau_1 \ \tau_2]^T$ and $\mathbf{d} = [\varepsilon \ \gamma_1 \ \gamma_2]^T$. The concept of effective stress $\tilde{\mathbf{s}} = \mathbf{E}_0(\mathbf{d} - \mathbf{d}_p)$ representing the stress of a fictitious undamaged material is introduced. These stresses are evaluated by solving a linear-hardening elasto-plastic problem considering the elastic stiffness matrix $\mathbf{E}_0 = \text{diag}\{E_n \ E_t \ E_t\}$, with E_n and E_t the elastic normal and shear moduli of the material, and the plastic strains ε_p . The nominal stress vector is obtained by multiplying the effective stress by the damage matrix $\mathbf{D} = \text{diag}\{D_n \ D_t \ D_t\}$, as given by:

$$\mathbf{s} = (\mathbf{I}_3 - \mathbf{D})\tilde{\mathbf{s}} = (\mathbf{I}_3 - \mathbf{D})\mathbf{E}_0(\mathbf{d} - \mathbf{d}_p) \quad (9)$$

The damage matrix contains the damage parameters in the normal (D_n) and shear (D_t) directions, ranging from 0 (no-damage) to 1 (complete damage). The damage evolution is governed by three ratios between the tensile, compressive and shear plastic works and the corresponding fracture energies ($G_t \ G_c \ G_s$). The damage in the normal direction assumes two different expressions in relation to the sign of the normal effective stress to allow the recovery of the normal stiffness in compression after the closure of tensile cracking [42].

Three plane yield surfaces define the elastic limits in shear (F_s) tension (F_t) and compression (F_c), as reported in the following:

$$F_s(\tilde{\sigma}, q) = \sqrt{\tilde{\tau}_1^2 + \tilde{\tau}_2^2} + \tilde{\sigma} \tan(\phi) - c' \quad (10)$$

$$F_t(\tilde{\sigma}, q) = \tilde{\sigma} - (f_t - q) \quad (11)$$

$$F_c(\tilde{\sigma}) = -\tilde{\sigma} + f_c \quad (12)$$

A 2D representation of the yield domain in the space $\tilde{\sigma} - \tilde{\tau} = \sqrt{\tilde{\tau}_1^2 + \tilde{\tau}_2^2}$ is reported in Fig. 3. In the expressions, f_t and f_c are the tensile and compressive material strengths, ϕ the friction angle and q a linear hardening variable, ranging from 0 (initial value) to the limit value $q_{lim} = \frac{c}{\tan(\phi)} - f_t$. Moreover, $c' = c$ if $q \leq q_{lim}$ and $c' = c + (q - q_{lim})\tan(\phi)$ if $q > q_{lim}$. With the increase of q , the surface F_t reduces until becoming a point when q reaches the value q_{lim} . On the other hand, F_s increases with the increase of q if $q > q_{lim}$. Two distinct associated plastic flows are defined for F_t and F_c , while a non-associated flow rule is assumed in shear employing a plastic potential (g_s), obtained from F_s substituting ϕ with ϕ_g , to take into account the effects of masonry dilatancy.

The complete formulation of the underlying constitutive model, including the hardening and the cyclic rules, can be found in [42].

The cyclic behaviour in tension is governed by the parameter ($\mu = \varepsilon_{p,f}/\varepsilon_f$), defined as the ratio between the residual normal strain ($\varepsilon_{p,f}$) when unloading from the point in which the full damage under pure tension ($D_n = 1$) is reached and the normal strain at that point (ε_f).

In this study, the model parameters of the constitutive law described above are evaluated following a simple calibration procedure, based on

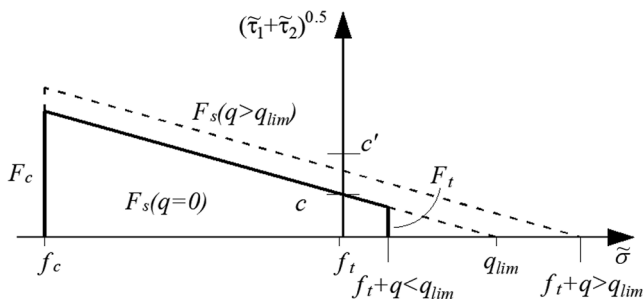


Fig. 3. Yield surface used for the ILs.

the mechanical properties of bricks and mortar joints or, alternatively, based on the corresponding mesoscale description of masonry. The elastic properties in the material local directions x - y , identifying the tangent plane of the masonry vault where a regular running bond is considered (Fig. 4a), are evaluated following the homogenisation technique proposed in [43]. The expressions of the equivalent normal and shear module $E_{nx}, E_{tx}, E_{ny}, E_{ty}$ are reported in the following expressions.

$$E_{nx} = \left[\frac{\mu_b}{E_b} + \frac{\mu_m}{E_m} - \frac{\mu_m \mu_b E_m E_b}{E_{ny}} \left(\frac{\nu_b}{E_b} - \frac{\nu_m}{E_m} \right)^2 \right]^{-1} \quad (13)$$

$$E_{ny} = \mu_m E_m + \mu_b E_b \quad (14)$$

$$E_{tx} = E_{ty} = 2 \left[\frac{2(1 + \nu_b)\mu_b}{E_b} + \frac{2(1 + \nu_m)\mu_m}{E_m} \right]^{-1} \quad (15)$$

where $\mu_m = \frac{h_m}{(h_m + h)}$; $\mu_b = \frac{h}{(h_m + h)}$; E_b, E_m are the Young's modulus of bricks and mortar; ν_b, ν_m are the Poisson's coefficients of bricks and mortar; b, h are the dimensions of the bricks and h_m is the average thickness of bed and head joints.

In the plane of the arch, a stack bond masonry, with no brick interlocking along the circumferential contact surfaces connecting the arch rings (Fig. 4b), is considered as it is a common solution adopted for multi-ring arches. Consistently to this, the equivalent normal and shear moduli along the local z direction, are evaluated by combining in-series the stiffness of bricks and mortar, results in:

$$E_{nz} = \frac{E_m E_b (h_z + h_{mz})}{E_b h_{mz} + E_m h_z} \quad (16)$$

$$E_{tz} = \frac{G_m G_b (h_z + h_{mz})}{G_b h_{mz} + G_m h_z} \quad (17)$$

where, h_z is the height of the bricks and h_{mz} the thickness of the circumferential joints.

The nonlinear parameters along the local x and z directions, are considered coincident to the nonlinear parameters of the mortar joints. Namely, the tensile strength (f_t), cohesion (c), friction factor (ϕ), and tensile and shear fracture energies normalised by the crack bandwidth ($\frac{G_t}{h_{cr}}, \frac{G_s}{h_{cr}}$) to ensure a mesh-independent response even in the presence of softening behaviour. The crack bandwidth, in each direction, is assumed as the minimum value between the mesh size and the dimension of the masonry unit in that direction. The influence of the mesh characteristics on the response prediction of masonry panels has been investigated in [41].

The nonlinear parameters along the local y direction (transversal direction of the vault) are evaluated according to [44] taking into

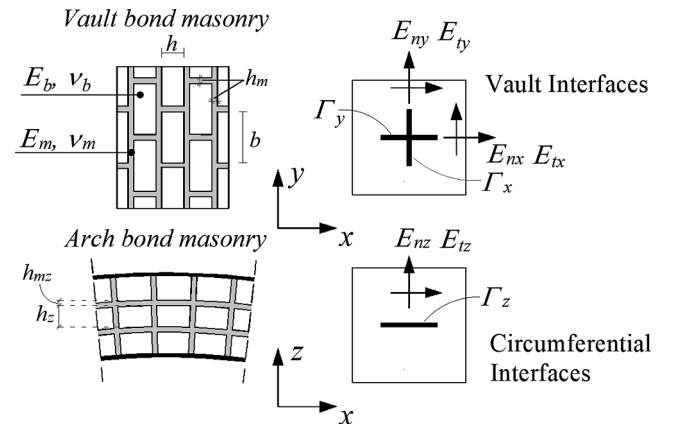


Fig. 4. Macroscopic homogenisation of the masonry periodic cell.

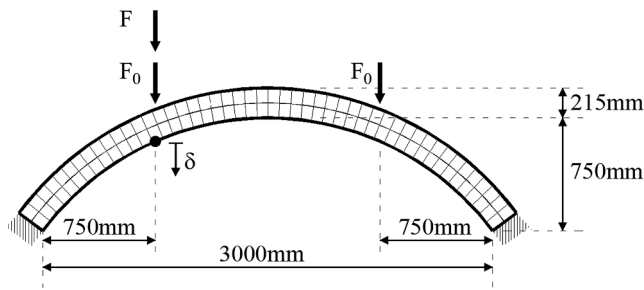


Fig. 5. Brick-masonry arch.

account the brick interlocking in this direction. The results are reported in Eqs. (18) and (19) where $r_b = b/2h$ and the subscripts j and b indicate the parameters of bricks and mortar joints, respectively. Finally, the masonry strength in compression, in each direction, is assumed as a macroscopic parameter to be evaluated from experimental tests carried out on masonry prisms.

$$f_{ry} = \min\{f_{ij} + c_j r_b \quad f_{ij} + f_{ib}/2\} \quad (18)$$

$$c_y = c_j \mu_m + c_b \mu_b \quad (19)$$

$$G_{ry} = \begin{cases} (G_{ij} + G_{sj} r_b)/(b + h_m) & \text{if } f_{ry} = f_{ij} + c_j r_b \\ (G_{ij} \mu_m + G_{ib} \mu_b)/(b + h_m) & \text{if } f_{ry} = f_{ij} \mu_m + f_{i,b} \mu_b \end{cases} \quad (20)$$

More accurate calibration procedures, based on 3D homogenisation techniques or numerical virtual tests, can be considered to improve the accuracy of the results. However, this task is beyond the scope of the present work which aims at investigating the accuracy and robustness of the proposed modelling strategy employing a simple calibration of the model parameters.

4. Verification, validation and application studies

The proposed macro-modelling strategy has been implemented in ADAPTIC [45], an advance FE code for nonlinear simulations of structures, and used to investigate the response of bare masonry arches, 3D vaults, and arches interacting with backfill under monotonic and cyclic loadings. The numerical results have been compared against detailed mesoscale simulations according the approach proposed in [46] and against experimental data reported in the literature.

4.1. 2D masonry arch

The first numerical-experimental comparison considers the two-ring brick-masonry arch, *Arch-G*, tested under vertical loading by Melbourne et al. [10]. The arch has 3 m span, 215 mm thickness and 455 mm width. It is made of class A engineering bricks $215 \times 102.5 \times 65 \text{ mm}^3$ arranged according to the stretcher bond with a continuous circumferential mortar joint connecting the two rings (Fig. 5). Mortar joints are 10 mm thick and characterised by a volumetric cement:lime:sand ratio of 1:2:9. In the physical test, rigid reinforced concrete abutments were used to avoid support movements. Two initial vertical forces $F_0 = 10 \text{ kN}$ each were applied at quarter and three-quarter span and kept constant during the test. Subsequently, a vertical force (F) at quarter span was increased up to collapse under force control (Fig. 5).

The developed mesoscale model is composed of 48 20-noded elastic

Table 2

Equivalent elastic properties of the macromodel [MPa].

Local direction z		Local direction x	
E_n	E_t	E_n	E_t
4818	4128	6956	3009

elements simulating the bricks of each arch ring. Nonlinear interface elements [46] are employed to describe the circumferential mortar joints connecting the two rings, and the bed mortar joints assumed as continuous along the radial directions. The mesoscale material parameters adopted in [47] are used. More specifically, the solid elements are characterised by a Young's modulus $E_b = 16000 \text{ MPa}$, a Poisson's ratio $\nu = 0.15$ and a specific self-weight of 22 kN/m^3 . The mechanical parameters for the nonlinear interfaces are reported in Table 1, where, k_n and k_t are the normal and tangential stiffnesses, f_b , f_c and c are the tensile strength, the compressive strength and the cohesion, ϕ and ϕ_g are the friction and dilatancy angles.

Two different macroscale models with 1×24 and 2×34 20-noded solid elements have been developed to assess the influence of the mesh size on the arch response prediction. The macroscale mechanical parameters have been determined following the procedure described in Section 3. The homogenised linear parameters are reported in Table 2, where the nonlinear properties coincide with the nonlinear material characteristics of the mesoscale interfaces in Table 1. Zero dilatancy angle is considered in the analysis according to [48]. However, this parameter is not expected to significantly affect the results since, as confirmed in the following numerical investigations, the failure mechanisms are not associated with sliding at the masonry joints. The effective lengths of 65 mm and 102.5 mm are used to normalise the fracture energies along the circumferential (x) and radial (z) directions, respectively.

Finally, the parameter μ governing the closure of the tensile cracks is assumed equal to 0.001, both in the mesoscale and macroscale description.

In the first simulation, the force F is monotonically increased reproducing the test protocol. The failure mechanisms obtained by the mesoscale model and the macroscale model with the finer mesh, with two solid elements along the thickness of the arch, are shown in Fig. 6, where the von-Mises equivalent stress contours are also displayed. The two alternative numerical descriptions predict the same flexural mechanism with the activation of four radial cracks, as observed in the experimental test. The load–deflection curves showing the variation of the vertical displacement δ at quarter span underneath the load are displayed in Fig. 7a. The macroscale curves obtained by using the two alternative meshes are in good agreement with the mesoscale response, confirming a negligible influence of the macroscale mesh characteristics. The macroscale model, however, overestimates the stiffness of the arch after 20kN of force and the peak load by about 15 % compared to the mesoscale and experimental results. A further study revealed that such discrepancy is associated with the contribution of the continuous circumferential mortar joint, which is spread along with the entire thickness of the arch in the simplified macroscale description. In fact, a mesoscale simulation for a single ring arch with the same geometrical and mechanical characteristics of the analysed two-ring masonry arch leads to a peak load very close to that predicted by the proposed macroscale model (Fig. 7a). Nevertheless, for displacement values larger

Table 1

Mechanical parameters of the mesoscale model.

k_n [N/mm ³]	k_t [N/mm ³]	f_t [MPa]	f_c [MPa]	c [MPa]	G_t [N/mm]	G_s [N/mm]	G_c [N/mm]	$tg\phi$ [–]	$tg\phi_g$ [–]
90.0	40.0	0.10	24.0	0.40	0.12	0.12	0.5	0.5	0.0

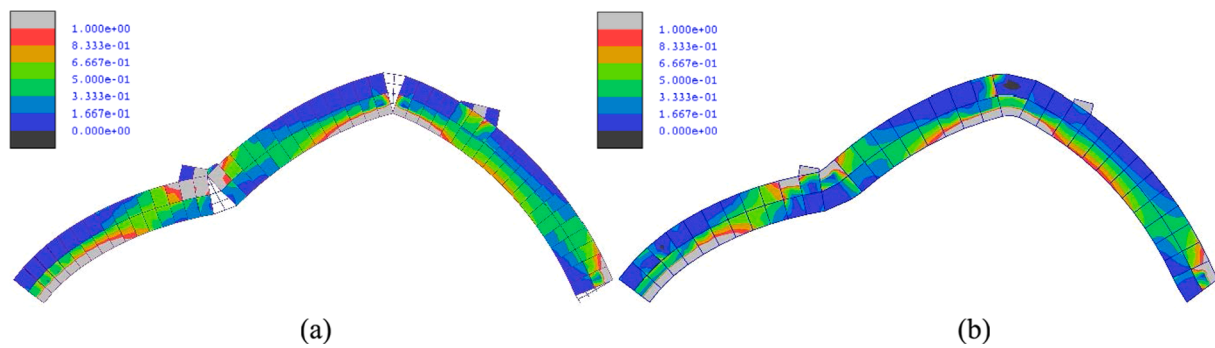


Fig. 6. Ultimate deformed shapes and Von-Mises stress distribution (in MPa) of the (a) mesoscale model and (b) macromodel.

than the peak-load displacement (about 2 mm), the two macroscale curves converge rapidly towards the mesoscale curve confirming an accurate prediction of the post-peak response.

In order to evaluate the ability of the proposed macroscale modelling strategy to predict the hysteretic behaviour of the arch, simulations under cyclic loading have been carried out using the 1×24 macroscale mesh and the mesoscale model. Four loading–unloading cycles with increasing maximum displacement (Fig. 7b) have been applied. The detailed mesoscale modelling strategy, which has been extensively validated in the literature (e.g. [42]), is considered here as the reference solution. The two models predict a very similar hysteretic behaviour characterised by the opening and closure of tensile cracks. The main difference is observed in terms of residual deformations which are larger for the macroscale model.

4.2. Arch interacting with backfill

In this section, the single-span masonry bridge specimen *Bridge 3–1* tested by Melbourne and Gilbert [12] is investigated using the proposed

macroscale modelling strategy. The analysed structure comprises a two-ring arch, backfill and spandrel walls. The arch is 2880 mm wide and has the same span, rise and thickness of the arch shown in Fig. 5 and considered in Section 4.1. The backfill extends horizontally 2460 mm from the two arch supports and is 300 mm deep at the arch crown. The *Bridge 3–1* specimen was subjected to a line load at the top surface of the backfill at the quarter span of the arch (Fig. 8). The load was uniformly distributed along the width of the bridge inducing a cylindrical deformation mode up to failure. The spandrel walls were detached from the arch, but they provided lateral confinement to the backfill.

The specimen was analysed by Zhang et al. [25] using a detailed mesoscale description explicitly allowing for the actual masonry bond. In this previous study, an efficient strip model representing a portion of the arch interacting with the backfill, which was fully restrained along the transverse direction, was adopted. A similar numerical model is used here, employing the same representation with 15-noded elasto-plastic tetrahedral elements for the backfill and a macroscale description for the arch, which corresponds to the coarser mesh with 1×24 20-noded solid elements introduced in Section 4.1. The adopted mesoscale and

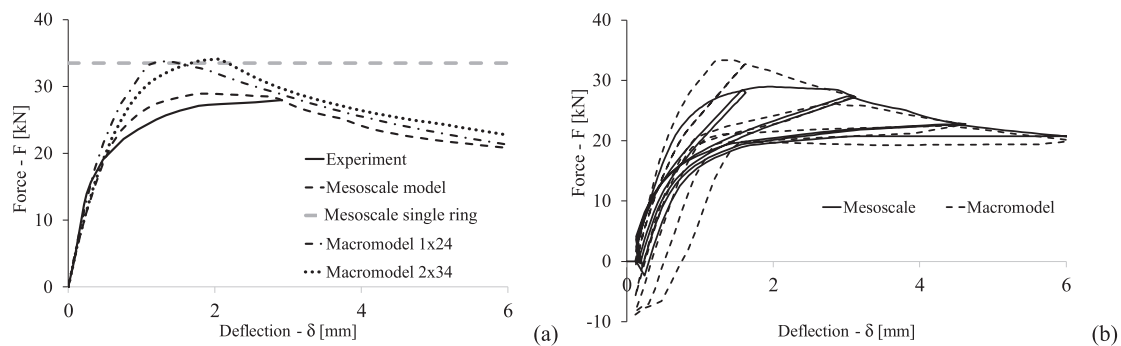


Fig. 7. Force deflection curves of the arch, considering (a) monotonic and (b) cyclic loading paths.

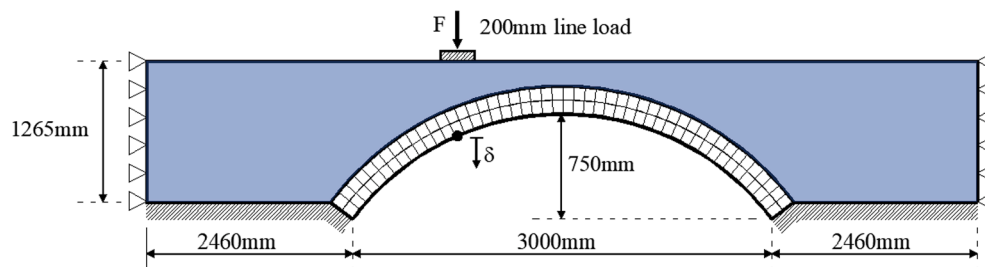


Fig. 8. Geometry of the prototype and test layout.

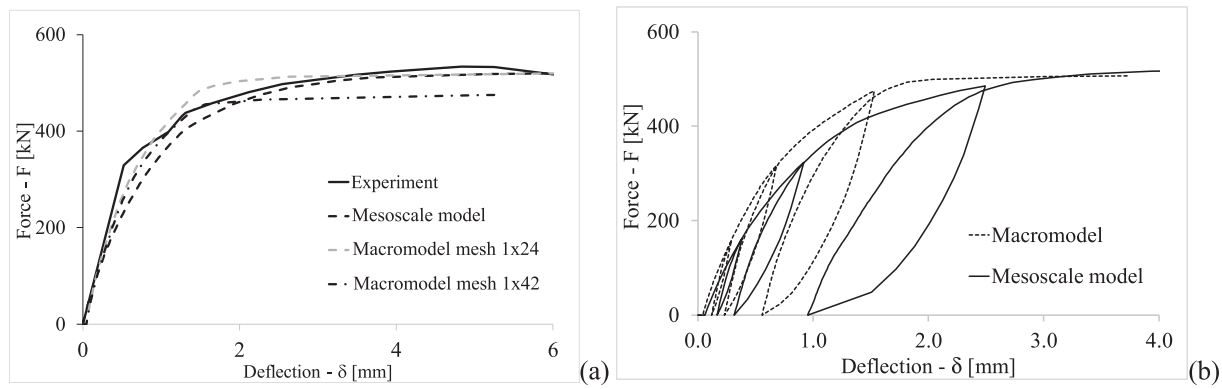


Fig. 9. Force-deflection curves of the arch interacting with backfill: (a) monotonic and (b) cyclic loading.

macroscopic masonry material properties are reported in Tables 1 and Table 2.

According to Zhang et al. [25], an elasto-plastic material model with a modified Drucker-Prager yield criterion is employed for the backfill, assuming a Young's modulus $E_b = 500$ MPa, a cohesion $c_b = 0.001$ MPa, friction and dilatancy coefficients $tg\phi_b = 0.95$ and $tg\psi_b = 0.45$, and a specific self-weight of 22 kN/m³. The interaction between the arch and the backfill is simulated by introducing nonlinear interfaces at the extrados of the arch with tensile strength $f_{ti} = 0.002$ MPa, cohesion $c_i = 0.0029$ MPa, friction coefficient $tg\phi_i = 0.6$ and zero dilatancy. The backfill domain is fully restrained at the two bases and longitudinally restrained at the two lateral faces to represent rigid supports. In addition, the nodes on the two longitudinal faces are transversally restrained to simulate the lateral confinement provided by the spandrel walls.

The monotonic load–deflection curve obtained by the macroscale mesh is shown in Fig. 9a, together with the experimental results and the mesoscale curve achieved adopting the same numerical description for the backfill. A very good agreement can be observed for displacement levels up to collapse. This improved accuracy compared to the results obtained for the bare masonry-two-ring arch in Section 4.1, especially in term of peak-load prediction, corroborates the critical role played by the backfill and the arch-backfill interaction on the load-carrying capacity of masonry arch bridges.

As for the bare arch in Section 4.1, further nonlinear simulations have been conducted considering a cyclic loading–unloading history. The macroscale and mesoscale curves are shown in Fig. 9b. Also, in the case of confined arch, the cyclic response of the macroscale model is in a good agreement with that predicted by the mesoscale model exhibiting a very similar hysteretic behaviour which is markedly different from that obtained for the bare arch, in section 4.1. This again emphasises the importance function of the backfill and the importance of a realistic hysteretic model for the backfill to effectively simulate the dissipative capacity of the composite arch-backfill system under cyclic loading conditions.

The results in Fig. 7 and Fig. 9 clearly show that load capacity of the bare arch is significantly reduced compared to that of the confined arch which may indicate a prevalent contribution of the backfill to the ultimate performance of the bridge specimen. However, as observed in Pantò et al. [34], a correct representation of the arch response is critical also in this case, as an inconsistent modelling of the masonry material of the arch may lead to an inaccurate representation of the arch-backfill interaction and unrealistic predictions of the actual failure mode and the resistance of the coupled arch-backfill system. Furthermore, it is important to point it out that the proposed macroscale masonry model enables accurate simulations of the monotonic and cyclic response of bare and confined arches without requiring sophisticated calibrations of the masonry material parameters, thus confirming the practicality and

the ease of use of the proposed macroscale masonry model for masonry arches and bridges.

Finally, Fig. 10 depicts the deformed shapes and the equivalent Von-Mises stresses for the mesoscale (Fig. 10a) and macroscale (Fig. 10b) models at collapse. In accordance with the experimental observations (e. g. [5,12]), both numerical models predict a flexural mechanism with general movement of soil beneath the load and on the side opposite to the loading area. Moreover, the two models predict significant sliding between the arch and backfill on the side opposite to the loading area. Fig. 10c and 10d show the damage index (ranging from 0 to 1) at the arch-backfill interfaces at the last step of the analyses.

4.3. Parametric analysis

To study the influence of the main model material parameters on the response under cyclic loading, parametric analyses have been carried out on both the bare two-ring masonry arch and the arch bridge specimen. The parameters considered in this numerical investigation have been selected amongst those that affect most the monotonic strength and stiffness of brick-masonry arches and bridges according to Tubaldi et al. [49]. In the case of the bare arch, the considered mesoscale material properties comprise the Young's modulus of the bricks (E_b), the normal stiffness (k_n), the tensile strength (f_t), the Mode-I fracture energy (G_t) and the residual strain factor (μ) of the nonlinear interface elements representing mortar joints, whereas in the analysis of the arch with backfill also the influence of the backfill cohesion (c_f) has been investigated. The ranges of variation of the model material parameters are summarised in Table 3. Nonlinear simulations under displacement control have been carried out changing one parameter at a time. It has been found that a variation of E_b and μ has only a marginal influence on the response predictions, but k_n , f_t , G_t and c_f are more influential.

Figs. 11 and 12 show mesoscale and macroscale load–displacement curves for the bare arch, respectively. It can be observed that both meso- and macroscale peak-load predictions are largely influenced by the variation of the tensile strength.

Furthermore, both models lead to residual load capacity values which are less dependent from material parameters (apart from the case of large fracture energy) which indicates that residual strength depends mostly on the geometrical characteristics of the arch and the level of precompression induced by the gravity loads directly applied onto it. Comparing mesoscale and macroscale responses, it can be observed that the proposed macroscale modelling strategy, apart from overestimating the peak-load, predicts also an initial steeper post-peak softening branch and larger residual plastic deformations after unloading. Finally comparing Figs. 11 and 12, it can be observed that the mesoscale peak load prediction is slightly less sensitive to the elastic stiffness and fracture energy. This may be explained considering the simplified

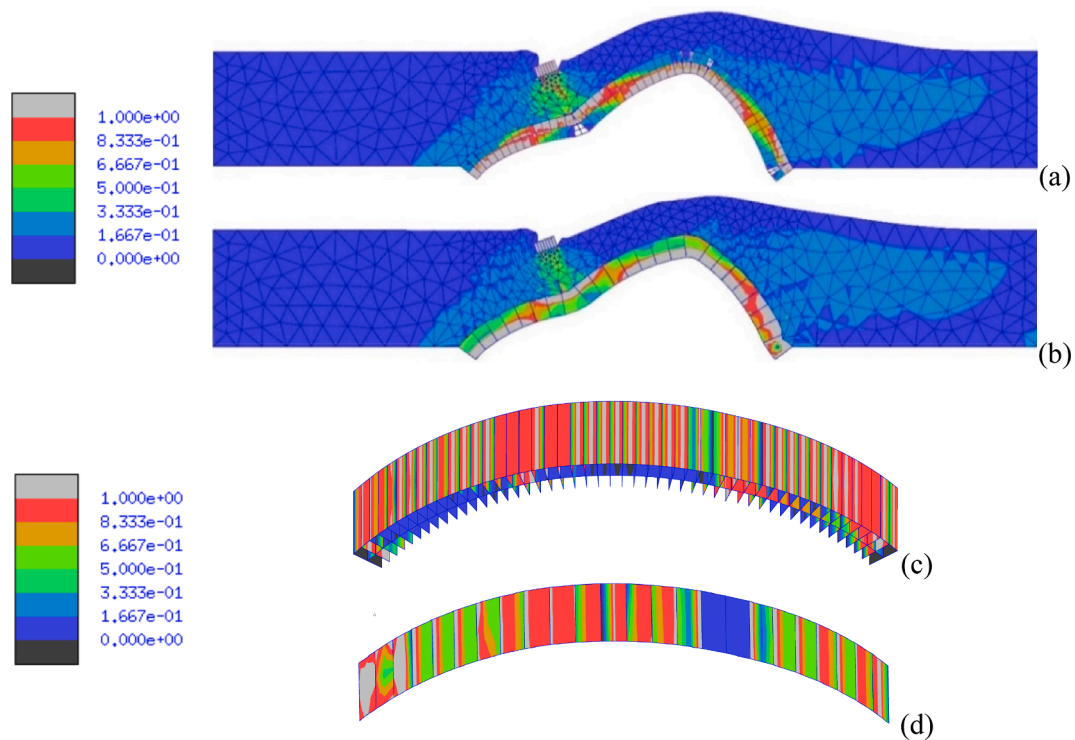


Fig. 10. Deformed shape and Von-Mises stresses (in MPa) at collapse: (a) mesoscale model and (b) macroscale model, and sliding damage at the arch-backfill interfaces predicted by the (c) mesoscale and the (d) macroscale model.

Table 3
Variation of the model material parameters.

E_b [GPa]		k_n [kN/mm ³]		f_t [MPa]		G_t [N/mm]		μ [-]		c_f [MPa]	
v_1	v_2	v_1	v_2	v_1	v_2	v_1	v_2	v_1	v_2	v_1	v_2
8	40	90	200	0.03	0.15	0.03	0.25	1E-4	0.1	5E-4	0.01

kinematics of the macro-model which spreads plastic deformations into a larger zone compared to the mesoscale model, making it more sensitive to variations of the stiffness and strength parameters.

Figs. 13 and 14 illustrate the main results obtained in the analysis of the arch with backfill. In this case, the backfill cohesion is the dominant parameter determining the peak load and the residual deformation upon unloading. Conversely, further parametric simulations, which are not reported here for the sake of brevity, indicates that the masonry parameters k_n , f_t , and G_t have a limited influence on the system response.

The numerical analyses have been performed by a displacement control algorithm, imposing the complete recovery of the applied displacement at the end of each cycle. Both mesoscale and macroscale curves are characterised by a mostly elasto-plastic behaviour with substantial residual deformations. This result is consistent with experimental observations on masonry arch bridge specimens subjected to vertical cyclic loading [5] and confirm the major role played by the backfill which reduces the effects of potential variations of the masonry material characteristics.

Furthermore, it can be observed from Figs. 13 and 14 that the initial stiffness is recovered at each cycle. This result is consistent with the damage-plasticity constitutive law adopted for interfaces, which is characterised by different damage indexes governing the material degradation in tension, compression and shear. More specifically, the system presents an increase of the initial stiffness by increasing the cycle amplitude. This result can be explained by the redistribution of internal forces between the arch and the backfill at the interface between the two domains due to residual sliding deformations.

4.4. 3D masonry vault

The accuracy and potential of the proposed macroscale modelling strategy has been assessed investigating also the response of a 3D masonry vault under static as well as dynamic (earthquake) loading. As for the previous cases, the macroscale predictions are compared against detailed mesoscale simulations which provide baseline results for model validation. The analysed masonry vault is 3 m wide and has the same span, rise and thickness of the arch shown in Fig. 5.

In the mesoscale model, the actual masonry bond along the transversal direction is also taken into account by representing each half brick with a 20-noded elastic element and alternating mortar interfaces with brick interfaces simulating the potential development of cracks within the bricks. The parameters reported in Table 1 are used for the mortar nonlinear interfaces, whereas the brick interfaces are characterised by high normal and shear stiffnesses $k_n = k_t = 10E5 \text{ N/mm}^3$ and by the following strength parameters: $f_t = 2.0 \text{ MPa}$, $G_t = 0.08 \text{ N/mm}$, $c = 2.8 \text{ MPa}$, $G_s = 0.5 \text{ N/mm}$, $f_c = 24.5 \text{ MPa}$, $G_c = 5.0 \text{ N/mm}$, according to [47]. The macroscopic material properties indicated in Table 4 have been evaluated following the procedure described in Section 3.

In initial simulations, the vault has been subjected to static patch loads applied on an area of $300 \times 400 \text{ mm}^2$, centred at three-quarter span (Fig. 15). In a first test, the monotonic load is applied vertically (F_v) and the vault is fully restrained at the two bases, while the two lateral faces are either free or restrained in the vertical direction to simulate the effects of rigid spandrel walls. Subsequently, the vault is analysed under horizontal cyclic forces (F_h) with fixed supports at the

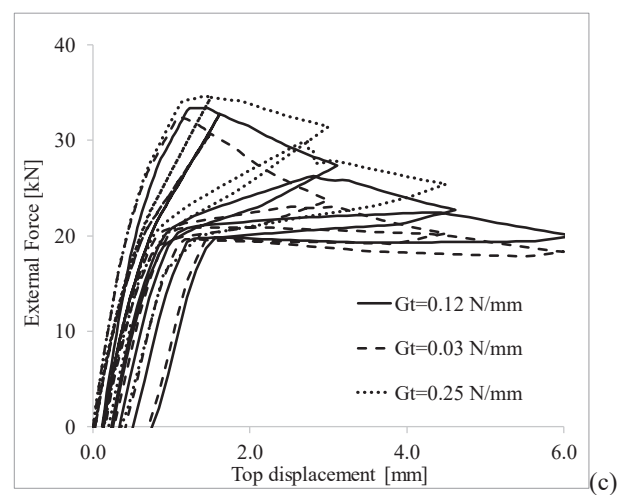
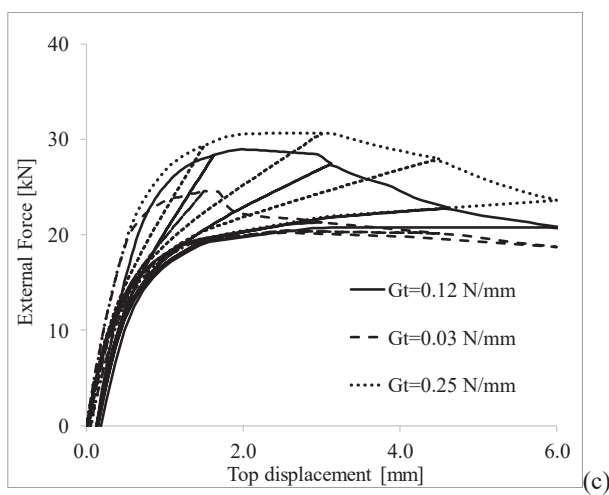
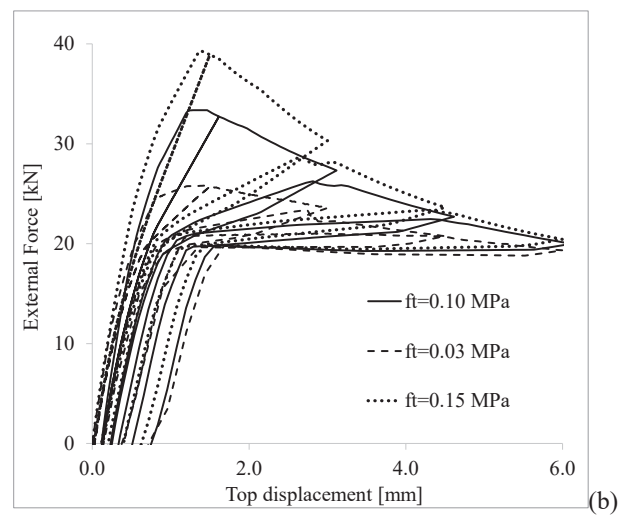
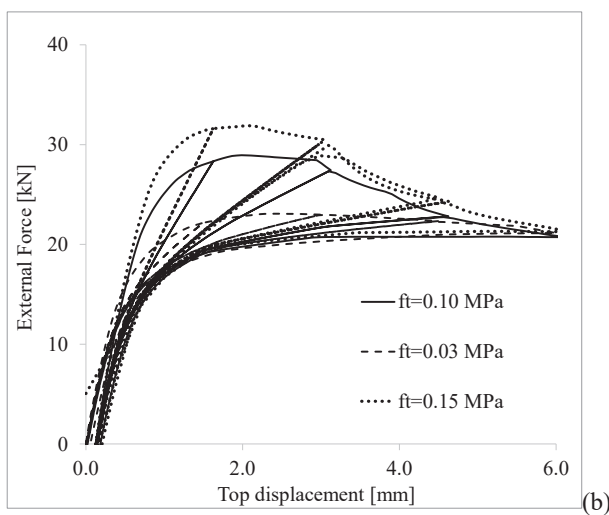
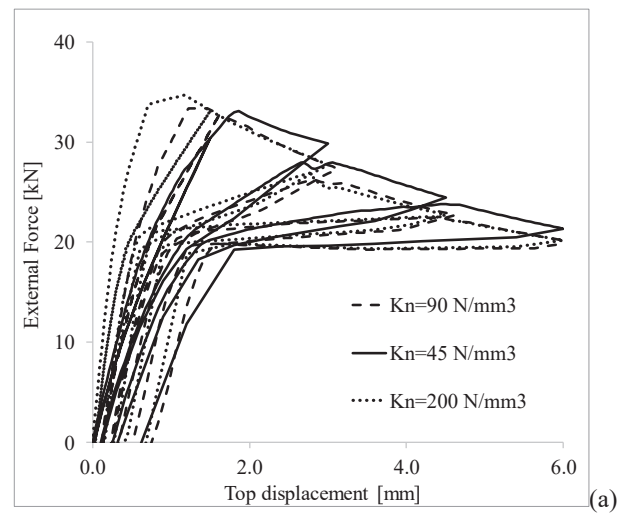
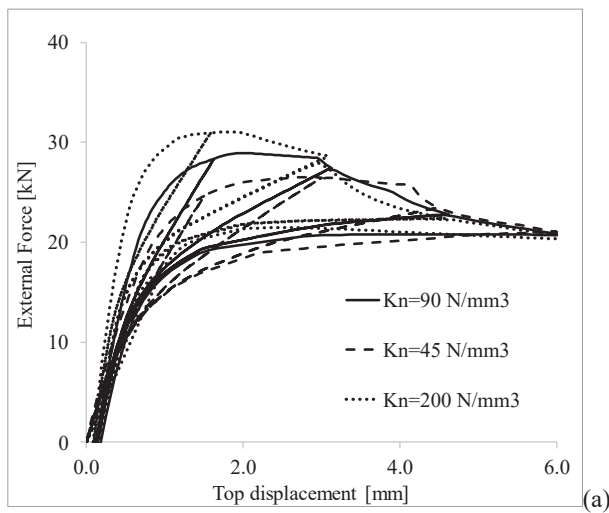


Fig. 11. Mesoscale parametric simulations on the two-ring arch based on the variation of: (a) the normal stiffness; (b) tensile strength; (c) fracture energy of the nonlinear interface elements representing mortar joints.

Fig. 12. Macroscale parametric simulations on the two-ring arch based on the variation of the normal stiffness (a) tensile strength (b) and fracture energy (c) of the nonlinear interface elements representing mortar joints.

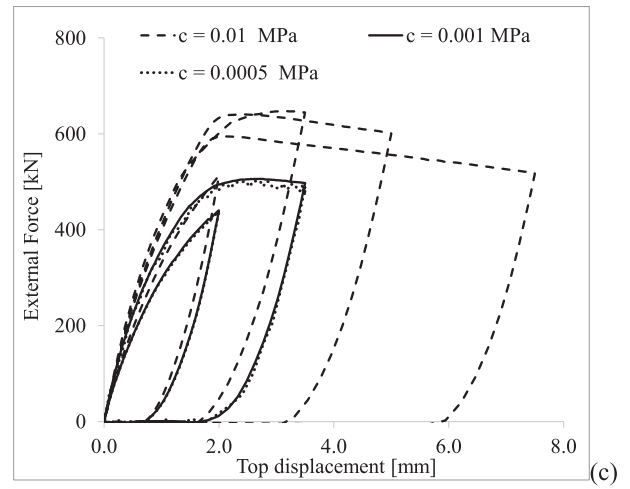
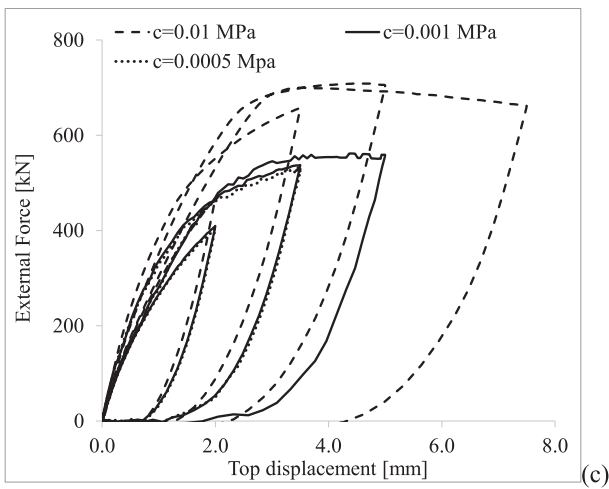
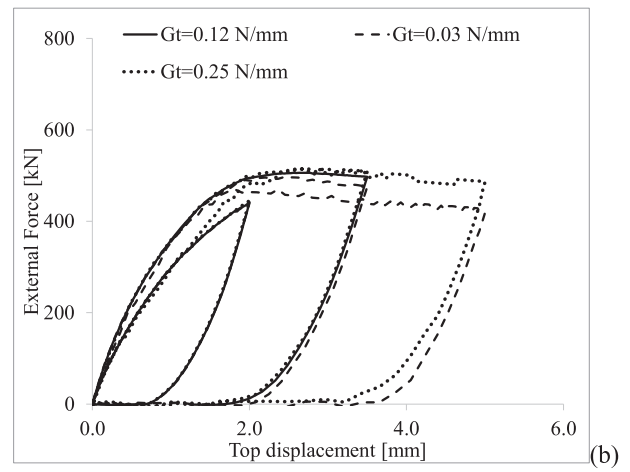
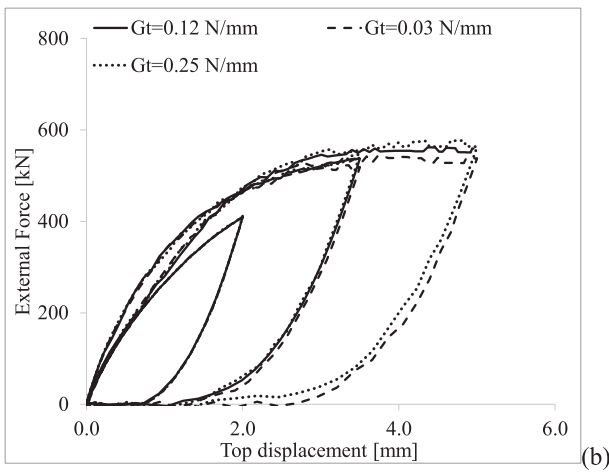
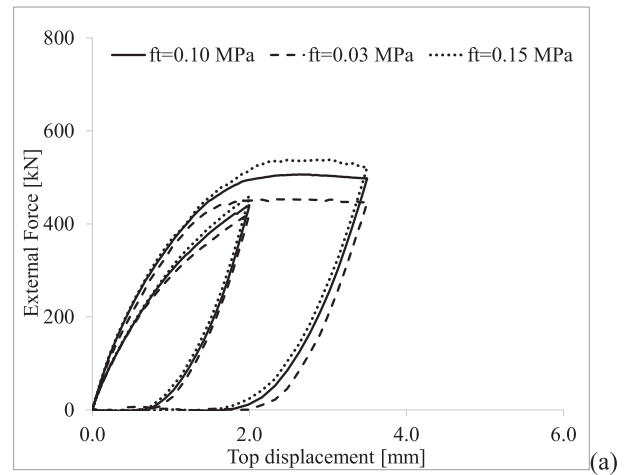
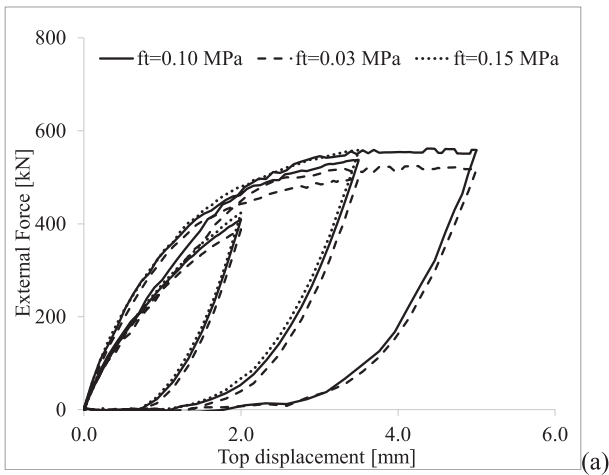


Fig. 13. Mesoscale parametric simulations on arch with backfill based on the variation of (a) tensile strength, (b) fracture energy and (c) backfill cohesion.

Fig. 14. Macroscale parametric simulations on arch with backfill based on the variation of (a) tensile strength, (b) fracture energy and (c) backfill cohesion.

Table 4
Mechanical properties adopted in the macromodel.

Local Direction	E_n [MPa]	E_t [MPa]	f_t [MPa]	f_c [MPa]	c [MPa]	G_t [N/mm]	G_s [N/mm]	G_c [N/mm]	$tg\phi$ [-]	$tg\phi_g$ [-]
x	4818	4128	0.10	24.5	0.40	0.10	0.125	5.0	0.50	0.0
y	13,980	4128	0.85	24.5	0.80	0.37	0.125	5.0	0.50	0.0
z	6956	3009	0.10	24.5	-	0.10	-	5.0	-	-

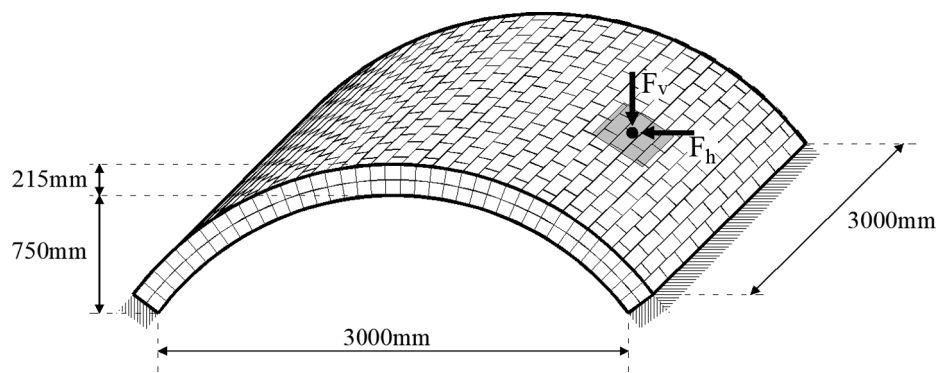


Fig. 15. 3D spatial vault prototypes.

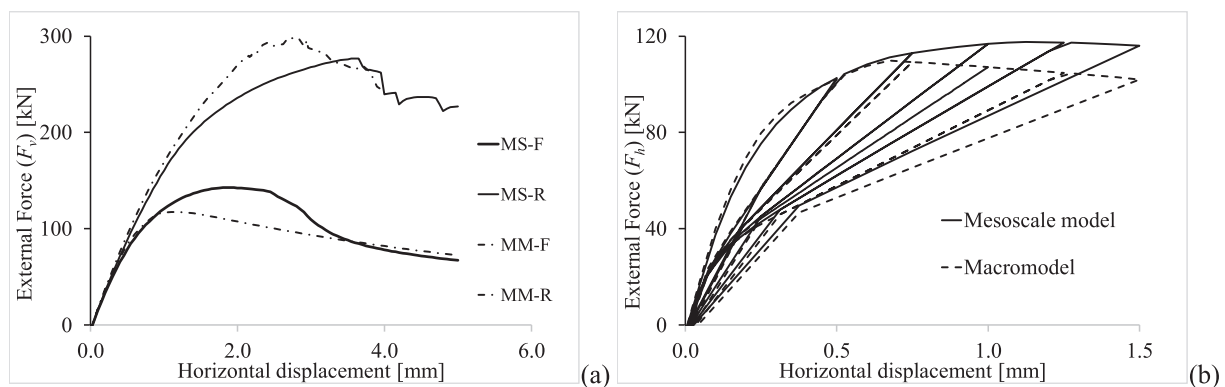


Fig. 16. Load-deflection curves for the masonry vault under (a) vertical monotonic and (b) horizontal cyclic loading.

bases and free at the two lateral faces.

The numerical load–deflection curves obtained in the two numerical experiments are presented in Fig. 16. More specifically, Fig. 16a displays the results associated with the monotonic vertical load F_v , while Fig. 16b shows the results for the horizontal cyclic load F_h .

In Fig. 16a, MS-F and MS-R refer to the response curves from mesoscale models with free and restrained lateral faces, respectively, while MM-F and MM-R denote the corresponding response curves obtained with the macroscale models. The restrained models show a load capacity which is approximately double that predicted by the models with free ends and a reduced ductility. The proposed macroscale modelling strategy offers a very accurate prediction of the initial stiffness and the residual resistance for the two different support conditions, but it underestimates of about 17 % the peak-load for the case with free end faces, and it overestimates the load capacity of about 7.5 % for the case with vertically restrained end faces. In Fig. 16a, the mesoscale model shows a more brittle post-peak behaviour caused by the activation of local ruptures at the interfaces, which is simulated by the macroscale model by the spread of the plastic deformations with the FE mesh.

A very good agreement between mesoscale and macroscale results under horizontal cyclic loading can be observed in Fig. 16b. This confirms that the proposed macroscale description enables a realistic representation of the cyclic hysteretic characteristics, including stiffness degradation and limited residual deformation upon unloading as predicted by the detailed mesoscale model.

Finally, the equivalent von-Mises stress distributions at the intrados and extrados of the vault with free end faces under vertical loading are

shown in Fig. 17. The stress pattern predicted by the macroscale model is consistent with that obtained by the mesoscale model, further confirming that the macroscale description leads to an accurate representation of 3D effects in masonry vaults.

In further numerical investigations, the vault has been subjected to prescribed acceleration histories at the two bases to represent the effects of earthquake loading. The N–S horizontal component of the Irpinia earthquake with PGA 0.32 g (Fig. 18) is simultaneously applied along the longitudinal and transversal directions of the vault. The earthquake record from Southern Italy Irpinia earthquake (1980), Sturmo station, is selected from the European Strong-Motion Database (ISESD), already processed by means of a linear baseline correction procedure and an eighth order elliptical bandpass filter with cut-off frequencies of 0.25 and 25.00 Hz [50,51].

A viscous damping proportional to the mass and associated with a damping coefficient $\xi = 1\%$ for a reference period of 0.10 s is employed in the nonlinear simulations. This considers the effects of potential micro-cracks that are not taken into account by the adopted material description improving numerical stability. The original signal has been scaled until the failure of the vault which was reached by both models for PGA = 2.56 g (8 times the original PGA) at approximately 5.3 s. The failure mode predicted by the mesoscale model is characterised by shear sliding along the radial joints at the vault bases (Fig. 19a). Extensive damage also develops along the vault span, as denoted by shear damage contours distribution at collapse shown in Fig. 19b.

A similar mechanism is predicted by the macroscale model as displayed in Fig. 20, where significant shear deformations localised at the

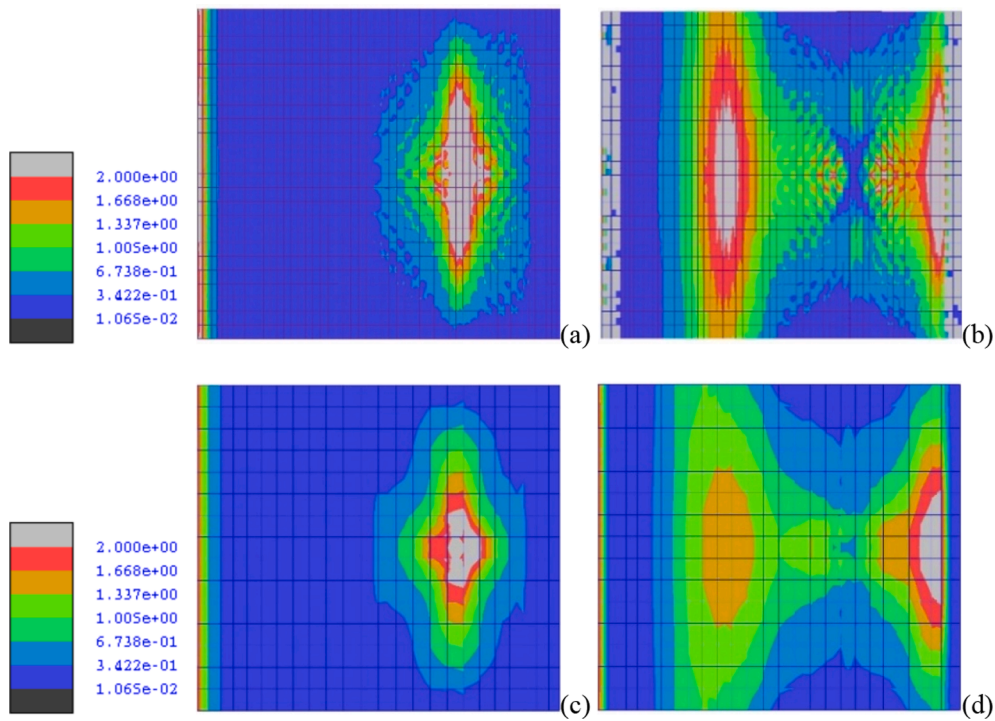


Fig. 17. Equivalent von Mises stresses (in MPa) at the peak-load for the vault with free ends under vertical loading: (a) extrados and (b) intrados of the mesoscale model and corresponding (c) extrados and (d) intrados of the macroscale description.

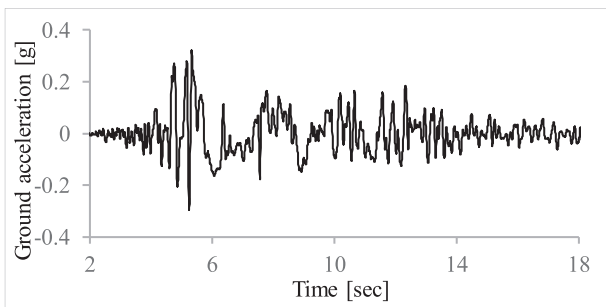


Fig. 18. Acceleration ground motion history applied in the analyses.

two supports.

Time-histories showing the variation in time of the relative longitudinal displacement centred at the crown of the vault, as predicted by the macroscale and mesoscale models for $PGA = 2.24\text{ g}$ and $PGA = 2.56\text{ g}$ (failure), are shown in Fig. 21a and b, respectively. Also these results confirm the potential of the macroscale strategy and its ability in

predicting the nonlinear dynamic response characteristics under earthquake loading, where the variation of peak displacements and frequencies are well simulated. The major differences from the mesoscale results can be noted from 6.0 s to 7.5 s, where the macroscale model shows higher high-frequency oscillations.

Finally, the hysteretic responses predicted by the two models for $PGA = 2.24\text{ g}$ and $PGA = 2.56\text{ g}$ are shown in Fig. 22, where the variation of the base shear along the longitudinal direction is plotted against the longitudinal horizontal displacement centred at the crown. A general good agreement between the two descriptions can be observed for $PGA = 2.24\text{ g}$ (Fig. 22a,b).

On the other hand, for $PGA = 2.56\text{ g}$, the macroscale model predicts wider hysteretic loops (Fig. 22c,d) which may be due to the nature of the failure mode with a concentration of shear sliding at the two ends of the vaults which is spread within continuous elements in the macroscale model, whereas it is concentrated at the nonlinear interfaces representing the radial joints in the mesoscale description.

The computational times of the two description strategies have been registered to evaluate the efficiency of the macroscale model compared to the more detailed mesoscale approach. Regarding the time history analysis with $PGA = 2.24\text{ g}$, the macromodel showed an average speed-

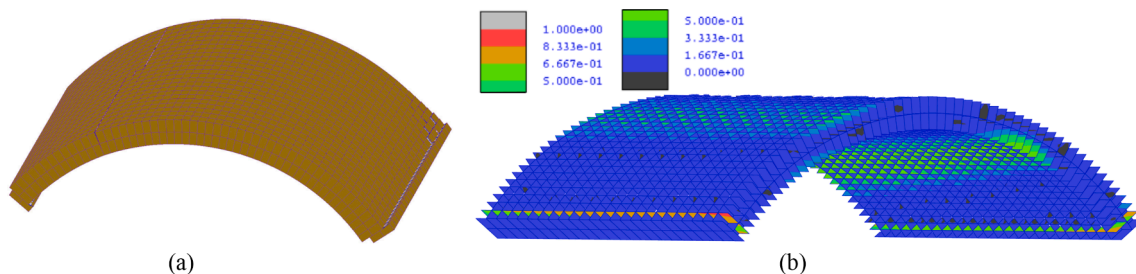


Fig. 19. Mesoscale model: (a) sliding failure mechanism of the vaults; (b) shear damage distribution at the interfaces.

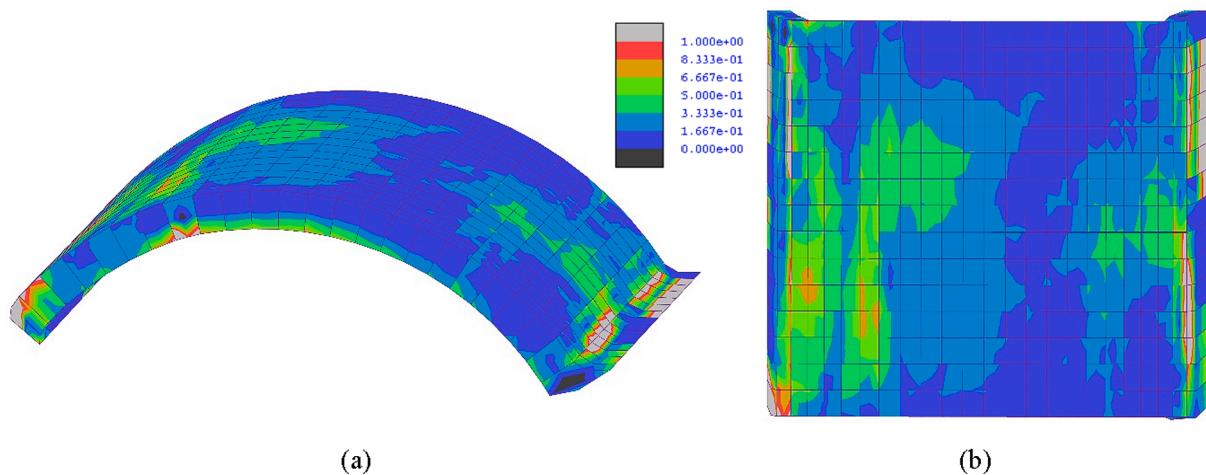


Fig. 20. Deformed shape and Von-Mises stress distribution (in MPa) of the macroscale model at collapse: (a) 3D and (b) top view.

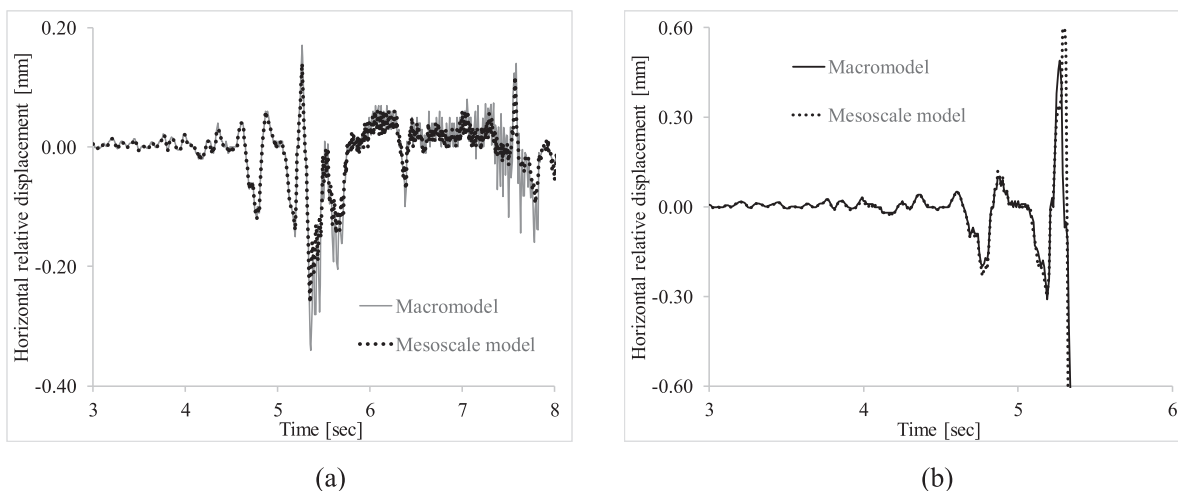


Fig. 21. Displacement time-histories displacement corresponding to the ground motion with (a) PGA 2.24 g and (b) PGA 2.56 g.

up value of approximately 83 %. This result demonstrates the high potentiality of the macromodel to be adopted for the simulation of large structures.

In the next validation, a further vault specimen with the same span, thickness and mechanical properties of the vault analysed in the previous example, but with a different span-to-rise ratio of 2.5, is investigated applying the same accelerogram in both longitudinal and transversal directions. The displacement time-histories for the macroscale and mesoscale descriptions and different levels of PGA are reported in Fig. 23. For $PGA = 0.32\text{ g}$ the two representations provide very similar responses. For higher values of PGA, 0.96 g and 1.60 g, the macromodel overestimates the displacement peaks, while providing a satisfactory prediction of the dynamic response of the vault in terms of frequencies of oscillation and predicting, coherently to the mesoscale model, the failure for a PGA of 1.60 g. The hysteretic cycles of the two models for PGA

$= 0.96\text{ g}$ and 1.60 g are reported in Fig. 24. The hysteretic characteristics of the macromodel are consistent with those predicted by the mesoscale model, but the macromodel tends to overestimate the amplitude of the hysteretic loops, leading to an overestimation of the effective energy dissipation capacity of the structure. Finally, the failure mechanisms obtained by the two models are reported in Fig. 25. In this case, a flexural failure mechanism is observed, which is due to the activation of four radial cracks. A very good agreement between the macroscale and mesoscale description can be observed.

4.5. Three-span masonry bridge

In this section, the response of a three-span arch bridge specimen, which was tested previously by Melbourne et al. [8] at the Bolton Institute (UK), is numerically simulated using the proposed macroscale

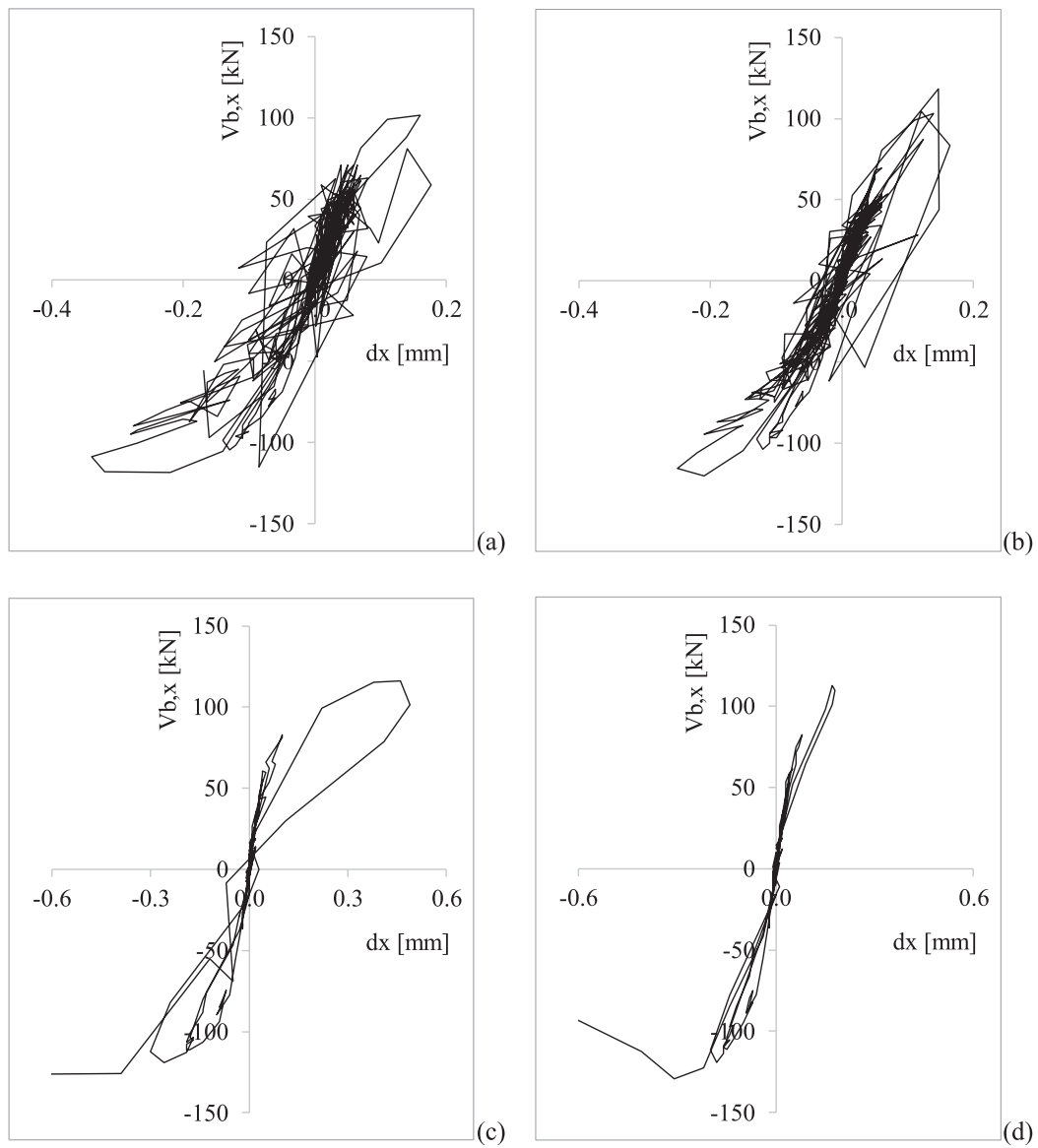


Fig. 22. Hysteretic curves for macromodel (a) and mesoscale model (b) at $PGA = 2.24$ g; macromodel (c) and mesoscale model (d) at $PGA = 2.56$ g.

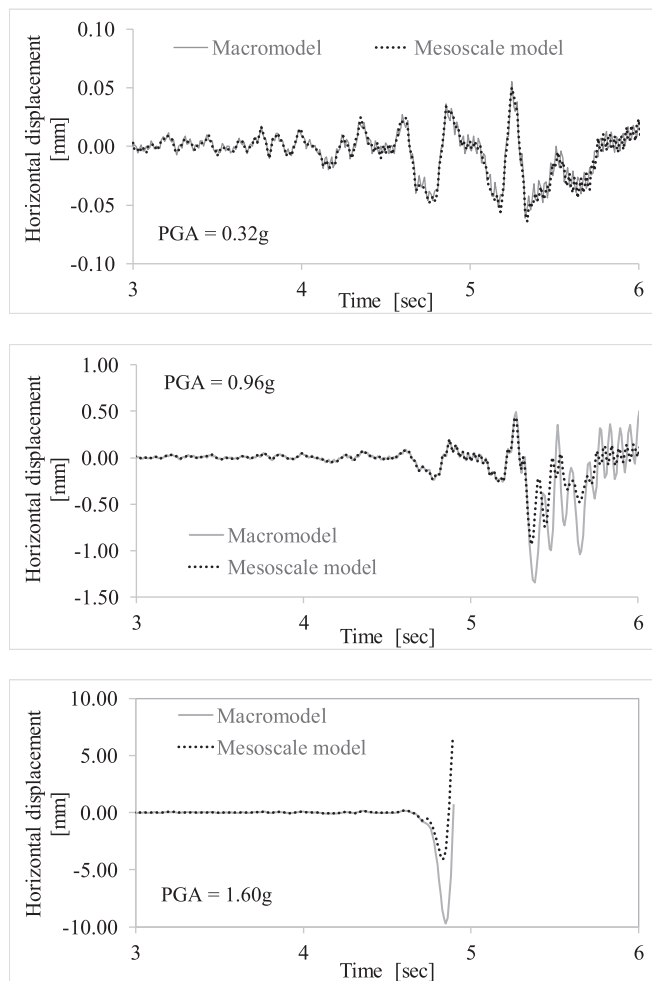


Fig. 23. Displacement time-histories for different levels of PGA.

model and the baseline detailed mesoscale model. The geometric characteristics of the analysed full-scale bridge specimen 2880 mm wide with detached spandrel walls (*Bridge-2* in [8]) is depicted in Fig. 26a.

The masonry of the specimen consists of class 'A' clay engineering bricks with 154 MPa compression strength and 1:2:9 (cement:lime:sand) mortar with 2.4 MPa compression strength. The masonry bond of the arches with two rings corresponds to that of the arch of the single span bridge specimen investigated in Section 4. The mechanical parameters of the brickwork and backfill obtained in material tests are summarised in Table 5.

Two strip models have been developed using the macro-scale (Fig. 26b) and the mesoscale (Fig. 26c) modelling approaches. For the mesoscale model, the same mesoscale material parameters utilised in Tubaldi et al. [49] are assumed. In particular, a Young's modulus of 18500 MPa and a Poisson's ratio of 0.15 are adopted for the solid elements, and the parameters indicated in Table 6 are employed for the nonlinear interfaces representing mortar joints. Following Tubaldi et al.

[49], the backfill is modelled utilising a Drucker-Prager criterion fitted to the inner edges of the Mohr-Coulomb yielding surface with a Young's modulus of 50 MPa, a Poisson's ratio of 0.20, a cohesion coefficient of 0.003 MPa and friction and dilatancy coefficients of 0.95 and 0.45, respectively. The backfill-masonry physical interface is modelled by nonlinear interfaces with negligible cohesion (0.001 MPa) and a friction coefficient of 0.6 according to [49]. Finally, the masonry macroscale parameters are evaluated based on the mesoscale parameters, according to the procedure described in Section 3. The equivalent macroscale elastic properties are listed in Table 7. The remaining parameters required to characterise the nonlinear behaviour of the macroscale internal layers are assumed to be equal to those adopted in the mesoscale model.

In a preliminary numerical investigation, the two alternative bridge models have been subjected to a vertical patch load applied at the quarter of the central span which is increased up to collapse following the loading protocol considered in experimental test. The patch load is applied considering a uniform load distribution on a patch area of $460 \times 2880 \text{ mm}^2$ using a displacement control algorithm.

Fig. 27 shows numerical and experimental load–displacement curves representing the variation of the vertical displacement at the intrados of the arch underneath the loaded area (Fig. 27a) and at the center of Span 3 (Fig. 27b) against the applied load. It can be seen that both the mesoscale and the macroscale model provide a realistic representation of the actual response, with predictions of initial stiffness, peak and residual loads very close to the experimental results. As a further comparison, Fig. 28 shows the numerical and experimental horizontal displacements at the top of the two piers. Again, both models simulate the experimental response with a high level of accuracy. The major differences are observed in the displacements at Pier 2, where the macroscale model underestimates the maximum top displacements of the pier.

Finally, Fig. 29 depict the deformed shapes of the two models at two levels of displacements with the distribution of von Mises stresses. The failure mechanisms predicted by the two numerical models are reasonably consistent with each other and consistent with the flexural failure mechanism observed in the test, Melbourne et al. [8], characterised by the formation of three plastic hinges (radial cracks in the arch) in the central span, two plastic hinges along Span 3, and a rocking mechanism of the Pier 2.

In a subsequent numerical investigation, an acceleration time-history is applied in the longitudinal direction at the base of the two piers and abutments and at the two end lateral surfaces of the bridge model. The same accelerogram shown in Fig. 18 is considered with an amplification factor of 2.0 (PGA 0.64 g) to represent a medium-strong earthquake. The displacements predicted by the mesoscale and the macroscale models are provided in Figs. 30 and 31, respectively. Three control points located at the mid-span section of the first, second and third arch (P_1 , P_2 , P_3), and the relative horizontal displacements at the top of two pier 1 (P_4) and pier 2 (P_5), are considered. The indexes (x) and (z) indicate, respectively, the relative horizontal the vertical displacements at the considered control points. A suitable agreement is observed between the responses predicted by the two alternative models up to collapse which occurs at around 5.4 sec.

Finally, the mesoscale and macroscale deformed shapes with equivalent von Mises stress contours at the last step of the numerical simulations are shown in Fig. 32a and 32b. A flexural shear failure mode is predicted by the mesoscale model. Flexural radial cracks and shear sliding separations are predicted to develop at the mortar interfaces at

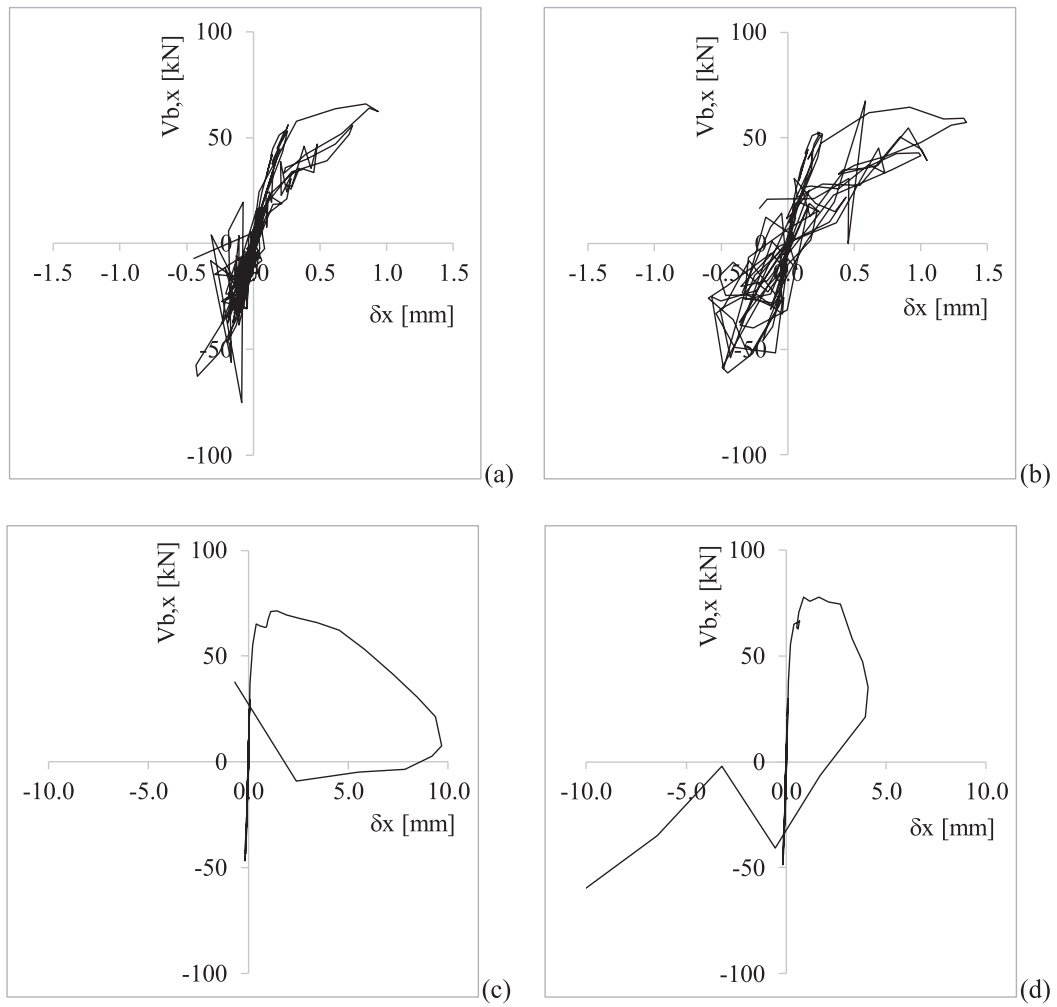


Fig. 24. Hysteretic curves for macromodel (a) and mesoscale model (b) at $PGA = 0.96$ g; macromodel (c) and mesoscale model (d) at $PGA = 1.60$ g.

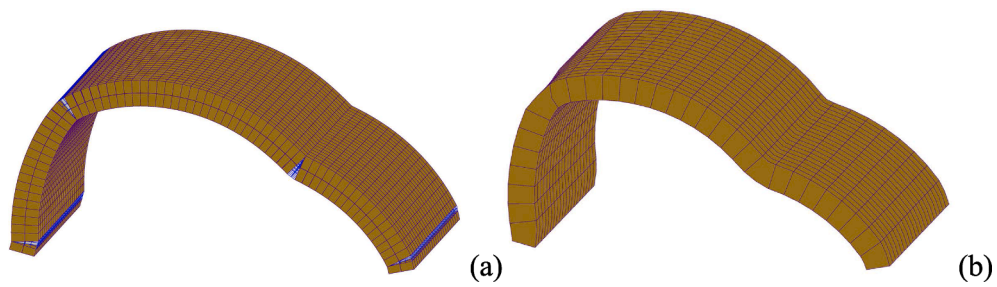


Fig. 25. Failure mechanism predicted by the mesoscale model (a) and the micromodel (b).

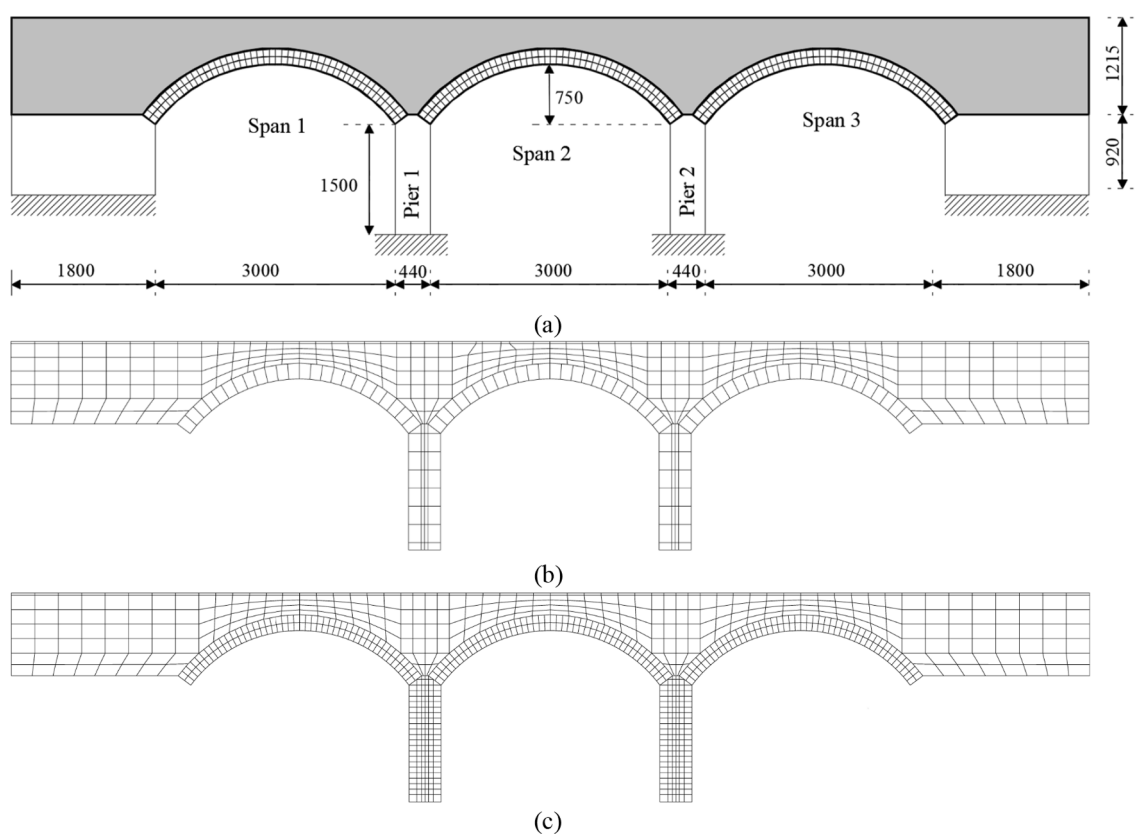


Fig. 26. The arch bridge specimen: (a) geometrical layout – dimensions in mm; (b) macroscale FE mesh; (c) mesoscale FE mesh.

Table 5
Masonry and backfill properties determined by material tests.

Bricks compression strength [MPa]	Mortar compression strength [MPa]	Masonry			Backfill		
		Compression strength [MPa]	Young's modulus [MPa]	Specific weight [kN/m ³]	Cohesion [MPa]	Friction angle [°]	Specific weight [kN/m ³]
154	2.4	26.8	16,200	22.4	0	60	22.2

Table 6
Mesoscale parameters adopted in the analyses [49].

k_n [N/mm ³]	k_t [N/mm ³]	f_t [MPa]	f_c [MPa]	c [MPa]	G_t [N/mm]	G_s [N/mm]	G_c [N/mm]	$\tan\phi$ [-]	$\tan\phi_g$ [-]	μ [-]
400	167	0.20	16.00	0.29	0.05	0.05	1.00	0.50	0.00	0.001

Table 7
Equivalent elastic properties of the macroscale model.

Element	Direction	E_n [Mpa]	E_t [Mpa]	f_t [Mpa]	c [Mpa]	G_t [N/mm]
Pier	Horizontal	10,860	9240	0.05	0.29	0.05
	Vertical	16,160		0.65	elastic	0.60
Arch	Circumferential	10,809	5620	0.05	0.29	0.05
	Radial	13,353				

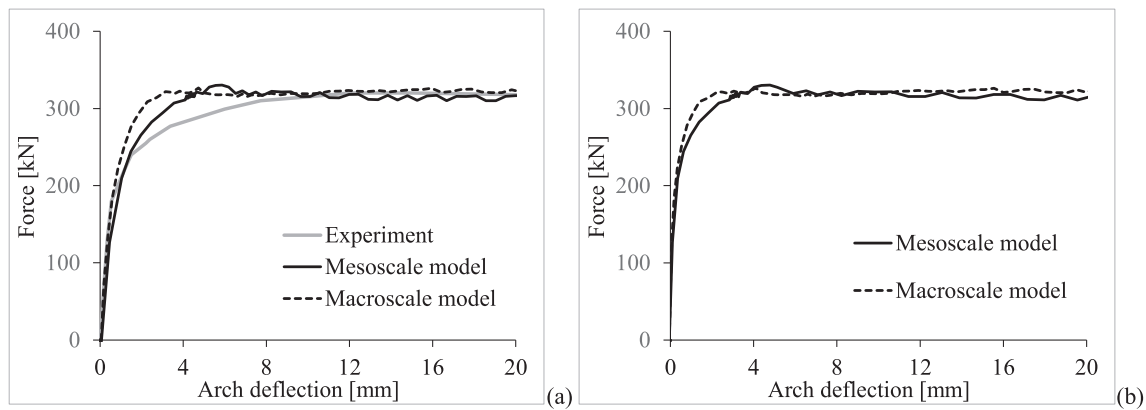


Fig. 27. Numerical and experimental load–displacement curves: (a) vertical displacement at quarter-span of the loaded arch; (b) vertical displacement at the centre of span 3.

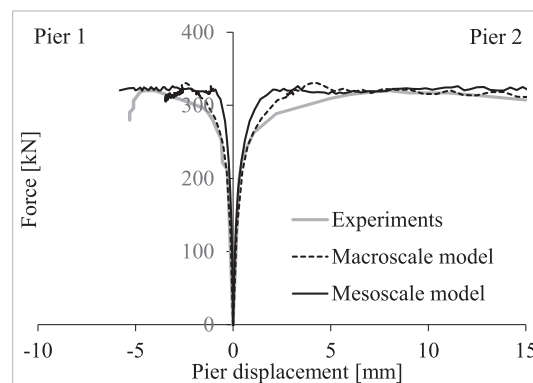


Fig. 28. Numerical and experimental load–displacement curves of the two piers.

different locations along the three arches and at the base of the two piers (Fig. 32a). Also in this case, the macroscale model reproduces the complex failure mechanism predicted by the more detailed mesoscale model with a good level of accuracy (Fig. 32b).

5. Conclusions

The paper presents a novel 3D macroscale modelling approach for the simulation of masonry arches, vaults and arch bridges under static and dynamic loading. The proposed modelling strategy is based on a 2-level description of the masonry. At the macroscopic level, masonry is simulated as a homogeneous continuum Cauchy domain, whilst at the local level the mesoscale structure of masonry is represented by means of a discrete distribution of embedded interfaces (internal layers) simulating tensile, shear and compressive plastic deformations of mortar joints and potential cracks within bricks. A simple but robust calibration procedure,

based upon the mesoscale mechanical parameters of masonry, is employed to evaluate the mechanical properties of the internal layers.

The proposed modelling strategy aims at providing an efficient but accurate numerical tool for the seismic assessment of large bridges with a reduced computational burden compared with detailed mesoscale descriptions. The model is validated with reference to 2D strip models of masonry arches, also interacting with a backfill layer, spatial vault specimens subjected to static and dynamic loading conditions, and a three-span bridge specimen. The results of the proposed model are compared to those obtained by detailed mesoscale models and experimental data, demonstrating the ability of the developed modelling strategy to simulate the cyclic and dynamic response of masonry arches and arch bridges. Further investigations considering entire masonry bridges, including spandrel walls and piers, will be considered in future research.

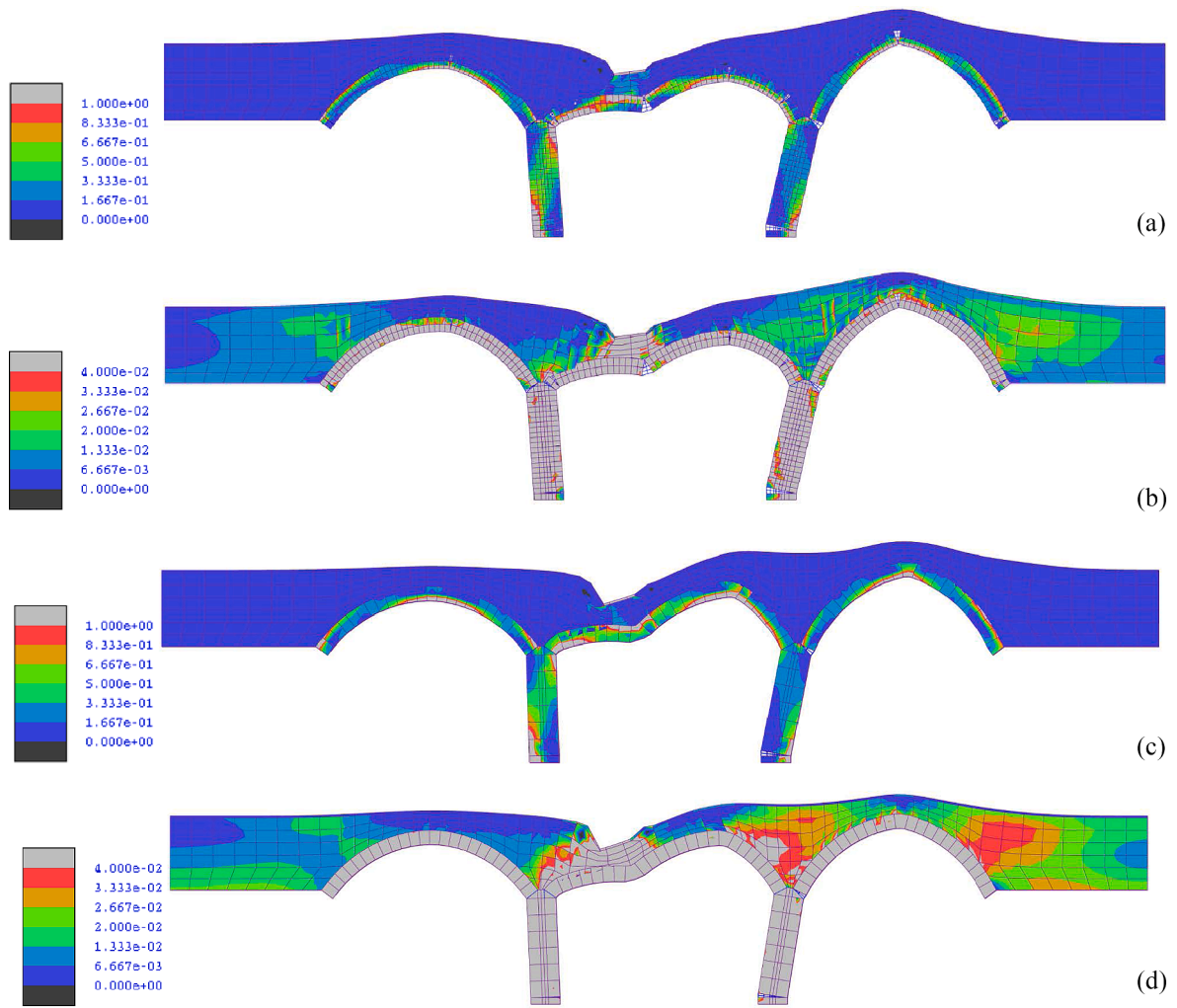


Fig. 29. Numerical failure mechanisms with von Mises stresses distributions (in MPa): Mesoscale model prediction at (a) 20 mm with 20 amplification factor and (b) 5 mm with amplification factor 60; macroscale prediction at (c) 20 mm with 20 amplification factor and (d) at 5 mm with amplification factor 60.

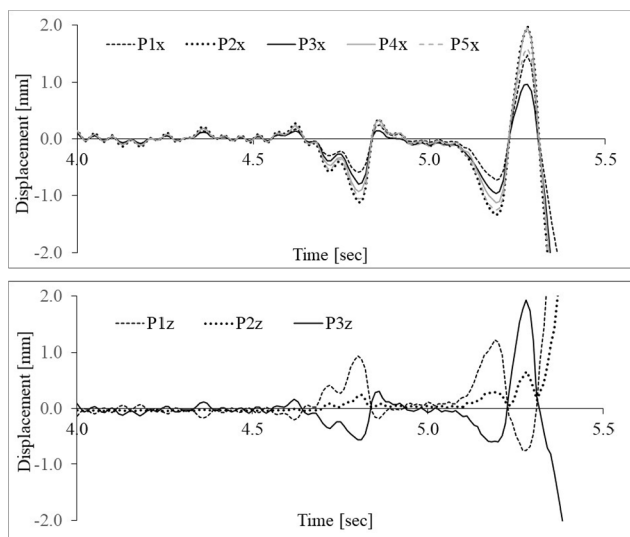


Fig. 30. Displacement time histories predicted by the mesoscale model.

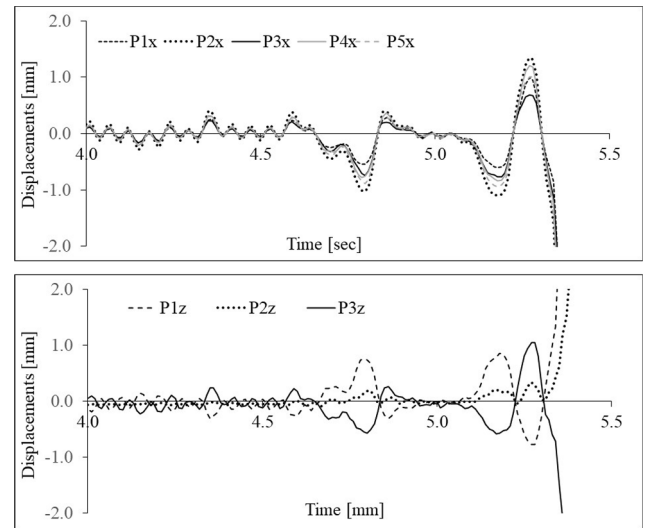


Fig. 31. Displacement time histories predicted by the macroscale model.

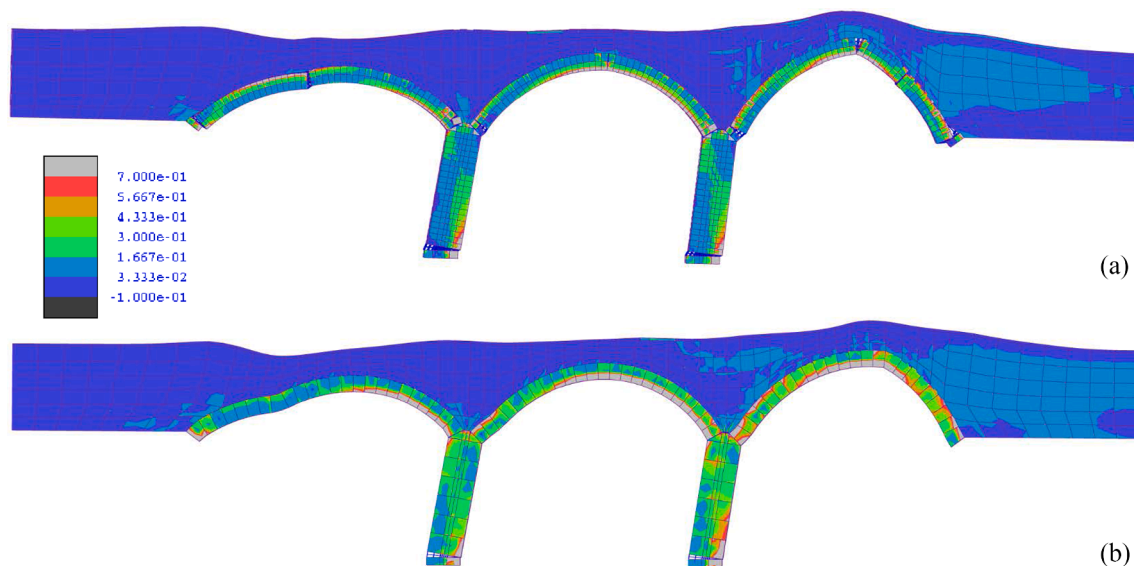


Fig. 32. Deformed shapes with von Mises stresses (in MPa) at the last step of the analysis predicted by the (a) mesoscale model and (b) macroscale model.

Funding

Funding was received for this work.

All of the sources of funding for the work described in this publication are acknowledged below:

Marie Skłodowska-Curie Individual fellowship under Grant Agreement 846061 (Project Title: Realistic Assessment of Historical Masonry Bridges under Extreme Environmental Actions, “RAMBEA”, <https://cordis.europa.eu/project/id/846061>).

Declaration of Competing Interest

The authors declare that they have no known competing financial interests or personal relationships that could have appeared to influence the work reported in this paper.

Data availability

No data was used for the research described in the article.

Acknowledgments

The authors gratefully acknowledge support from the Marie Skłodowska-Curie Individual fellowship under Grant Agreement 846061 (Project Title: Realistic Assessment of Historical Masonry Bridges under Extreme Environmental Actions, “RAMBEA”, <https://cordis.europa.eu/project/id/846061>).

References

- Melbourne C, McKibbins LD, Sawar N, Gaillard CS. Masonry arch bridges: condition appraisal and remedial treatment. London: CIRIA; 2006.
- Ural A, Oruç Ş, Doğançın A, Tuluk Öİ. Turkish historical arch bridges and their deteriorations and failures. *Eng Fail Anal* 2008 Jan 1;15(1–2):43–53.
- Oliveira DV, Lourenço PB. Repair of stone masonry arch bridges. In: Proceedings of the 4th International Conference on Arch Bridges. Barcelona, Spain: CIMNE; 2004.
- Sarhosis V, De Santis S, de Felice G. A review of experimental investigations and assessment methods for masonry arch bridges. *Struct Infrastruct Eng* 2016;12(11):1439–64.
- Augustus-Nelson L, Swift G, Melbourne C, Smith C, Gilbert M. Large-scale physical modelling of soil-filled masonry arch bridges. *Int J Phys Model Geotech* 2018;18(2):81–94.
- Callaway P, Gilbert M, Smith CC. Influence of backfill on the capacity of masonry arch bridges. In: Proceedings of the institution of civil engineers-bridge engineering, vol. 165 (3). Thomas Telford Ltd; 2012. p. 147–157.
- Gilbert M, Smith CC, Wang J, Callaway PA, Melbourne C. Small and large-scale experimental studies of soil-arch interaction in masonry bridges. In: 5th international conference on arch bridges ARCH, vol. 7; 2007. p. 381–388.
- Melbourne C, Gilbert M, Wagstaff M. The collapse behaviour of multispan brickwork arch bridges. *Struct Eng* 1997;75(17).
- Royles R, Hendry AW. Model tests on masonry arches. *Proc Inst Civ Eng* 1991;91(2):299–321.
- Melbourne C, Holm G, Bien J, Casas JR, Tommor A, Bengtsson PE, Kaminski T, Rawa P, Roca P, Molins C. Masonry arch bridges: sustainable bridges background document 4.7.
- Melbourne C, Tomor AK, Wang J. Cyclic load capacity and endurance limit of multi-ring masonry arches. In: Proceedings of the 4th international conference on arch bridges. Barcelona, Spain: CIMNE; 2004. p. 375–384.
- Melbourne C, Gilbert M. The behaviour of multiring brickwork arch bridges. *Struct Eng* 1995;73(3).
- Gattesco N, Boem I, Andretta V. Experimental behaviour of non-structural masonry vaults reinforced through fibre-reinforced mortar coating and subjected to cyclic horizontal loads. *Eng Struct* 2018;1(172):419–31.
- Giamundo V, Lignola GP, Maddaloni G, Da Porto F, Prota A, Manfredi G. Shaking table tests on a full-scale unreinforced and IMG-retrofitted clay brick masonry barrel vault. *Bull Earthq Eng* 2016;14(6):1663–93.
- Cavicchi A, Gamberotta L. Collapse analysis of masonry bridges taking into account arch–fill interaction. *Eng Struct* 2005;27(4):605–15.
- Gilbert M, Nguyen DP, Smith CC. Computational limit analysis of soil-arch interaction in masonry arch bridges. In Proceedings of the 5th international conference on arch bridges, Madeira, Portugal, vol. 7; 2007. p. 633–640.
- Zampieri P, Zanini MA, Faleschini F. Derivation of analytical seismic fragility functions for common masonry bridge types: methodology and application to real cases. *Eng Fail Anal* 2016;1(68):275–91.
- Audenaert A, Fanning P, Sobczak L, Peremans H. 2-D analysis of arch bridges using an elasto-plastic material model. *Eng Struct* 2008;30(3):845–55.
- Gago AS, Alfaiate J, Lamas A. The effect of the infill in arched structures: Analytical and numerical modelling. *Eng Struct* 2011;33(5):1450–8.
- Sarhosis V, Forgács T, Lemos JV. A discrete approach for modelling backfill material in masonry arch bridges. *Comput Struct* 2019;1(224):106108.
- Thavalingam A, Bicanic N, Robinson JI, Ponniah DA. Computational framework for discontinuous modelling of masonry arch bridges. *Comput Struct* 2001;79(19):1821–30.
- Fanning PJ, Boothby TE. Three-dimensional modelling and full-scale testing of stone arch bridges. *Comput Struct* 2001;79(29–30):2645–62.
- Milani G, Lourenço PB. 3D non-linear behavior of masonry arch bridges. *Comput Struct* 2012;1(110):133–50.
- Conde B, Ramos LF, Oliveira DV, Riveiro B, Solla M. Structural assessment of masonry arch bridges by combination of non-destructive testing techniques and three-dimensional numerical modelling: Application to Vilanova bridge. *Eng Struct* 2017;1(148):621–38.
- Zhang Y, Tubaldi E, Macorini L, Izzuddin BA. Mesoscale partitioned modelling of masonry arches allowing for arch-backfill interaction. *Constr Build Mater* 2018;10(173):820–42.
- Tubaldi E, Macorini L, Izzuddin BA. Three-dimensional mesoscale modelling of multi-span masonry arch bridges subjected to scour. *Eng Struct* 2018;15(165):486–500.

- [27] Pulatsu B, Erdogmus E, Lourenço PB. Comparison of in-plane and out-of-plane failure modes of masonry arch bridges using discontinuum analysis. *Eng Struct* 2019;178:24–36.
- [28] Caddemi S, Caliò I, Cannizzaro F, D'Urso D, Occhipinti G, Pantò B, et al. A parsimonious 3D Discrete Macro-Element method for masonry arch bridges. In: *Proceedings of 10th IMC, international masonry conference, 2018 July, Milan, Italy*.
- [29] Zampieri P, Zanini MA, Modena C. Simplified seismic assessment of multi-span masonry arch bridges. *Bull Earthq Eng* 2015;13(9):2629–46.
- [30] Pelà L, Aprile A, Benedetti A. Comparison of seismic assessment procedures for masonry arch bridges. *Constr Build Mater* 2013;38:381–94.
- [31] Pelà L, Aprile A, Benedetti A. Seismic assessment of masonry arch bridges. *Eng Struct* 2009;31(8):1777–88.
- [32] DIANA FEA, 2017. *DIANA User's Manual – Release 10.1*. Delft, Netherlands.
- [33] Chisari C, Macorini L, Izzuddin BA. Multiscale model calibration by inverse analysis for nonlinear simulation of masonry structures under earthquake loading. *Int J Multiscale Comput Eng* 2020;18(2).
- [34] Pantò B, Chisari C, Macorini L, Izzuddin BA. A hybrid macro-modelling strategy with multi-objective calibration for accurate simulation of multi-ring masonry arches and bridges. *Comput Struct* 2022;265:106769.
- [35] Bertolesi E, Adam JM, Rinaudo P, Calderón PA. Research and practice on masonry cross vaults—A review. *Eng Struct* 2019;180:67–88.
- [36] Milani G, Tralli A. A simple meso-macro model based on SQP for the non-linear analysis of masonry double curvature structures. *Int J Solids Struct* 2012;49(5): 808–34.
- [37] Bertolesi E, Milani G, Casolo S. Homogenization towards a mechanistic Rigid Body and Spring Model (HRBSM) for the non-linear dynamic analysis of 3D masonry structures. *Meccanica* 2018;53(7):1819–55.
- [38] Bertolesi E, Silva LC, Milani G. Validation of a two-step simplified compatible homogenisation approach extended to out-plane loaded masonries. *Int J Masonry Res Innovation* 2019;4(3):265–96.
- [39] Sarhosis V, Oliveira DV, Lemos JV, Lourenço PB. The effect of skew angle on the mechanical behaviour of masonry arches. *Mech Res Commun* 2014;61:53–9.
- [40] Cannizzaro F, Pantò B, Caddemi S, Caliò I. A Discrete Macro-Element Method (DMEM) for the nonlinear structural assessment of masonry arches. *Eng Struct* 2018;168:243–56.
- [41] Pantò B, Macorini L, Izzuddin BA. A two-level macroscale continuum description with embedded discontinuities for nonlinear analysis of brick/block masonry. *Comput Mech* 2022;69(3):865–90.
- [42] Minga E, Macorini L, Izzuddin BA. A 3D mesoscale damage-plasticity approach for masonry structures under cyclic loading. *Meccanica* 2018;53(7):1591–611.
- [43] Gambarotta L, Lagomarsino S. Damage models for the seismic response of brick masonry shear walls. Part I: the mortar joint model and its applications. *Earthquake Eng Struct Dyn* 1997;26(4):423–39.
- [44] Lourenço PB, De Borst R, Rots JG. A plane stress softening plasticity model for orthotropic materials. *Int J Numer Meth Eng* 1997;40(21):4033–57.
- [45] Izzuddin BA. *Nonlinear dynamic analysis of framed structures*, PhD thesis. London, UK: Imperial College London; 1991.
- [46] Macorini L, Izzuddin B. A non-linear interface element for 3D mesoscale analysis of brick-masonry structures. *Int J Numer Meth Eng* 2011;85(12):1584–608.
- [47] Zhang Y, Macorini L, Izzuddin BA. Mesoscale partitioned analysis of brick-masonry arches. *Eng Struct* 2016;124:142–66.
- [48] Van der Pluijm R. *Out-of-plane bending of masonry behaviour and strength*, PhD thesis. Eindhoven, Netherland: Eindhoven University of Technology; 1999.
- [49] Tubaldi E, Macorini L, Izzuddin BA. Identification of critical mechanical parameters for advanced analysis of masonry arch bridges. *Struct Infrastruct Eng* 2020;16(2):328–45.
- [50] Ambraseys N, Smit P, Douglas J, Margaris B, Sigbjörnsson R, Olafsson S, et al. Internet site for European strong-motion data. *Bollettino di geofisica teorica ed applicata* 2004;45(3):113–29.
- [51] Ambraseys N, Smit P, Douglas J, Margaris B, Sigbjörnsson R, Olafsson S, et al. Internet site for European strong-motion data. *Bollettino di geofisica teorica ed applicata* 2004;45(3):113–29.